Brain Research Bulletin 234 (2026) 111685

Contents lists available at ScienceDirect

Brain Research Bulletin

journal homepage: www.elsevier.com/locate/brainresbull

Research report

Reversal of auditory cortical hyperexcitability and restoration of synaptic plasticity balance by GluN1-mediated photobiomodulation in noise-induced tinnitus

Zhixin Zhang [a,b,c,d,e,f,1,2], Xinmiao Xue [a,b,c,d,e,f,1], Dongdong He [a,b,c,d,e,f,1], Peng Liu [a,b,c,d,e,g,1], Chi Zhang [a,b,c,d,e], Yvke Jiang [a,b,c,d,e,f], Shuhan Lv [a,b,c,d,e,f], Li Wang [a,b,c,d,e,f], Hanwen Zhou [a,b,c,d,e], Weidong Shen [a,b,c,d,e], Shiming Yang [a,b,c,d,e,*], Fangyuan Wang [a,b,c,d,e,*]

[a] Senior Department of Otolaryngology Head and Neck Surgery, The sixth of Chinese PLA General Hospital, Chinese PLA Medical School, Beijing 100853, China
[b] State Key Laboratory of Hearing and Balance Science, Beijing 100853, China
[c] National Clinical Research Center for Otolaryngologic Diseases, Beijing 100853, China
[d] Key Laboratory of Hearing Science, Ministry of Education, Beijing 100853, China
[e] Beijing Key Laboratory of Hearing Impairment Prevention and Treatment, Beijing 100853, China
[f] Graduate School of Medicine, Chinese PLA General Hospital, Chinese PLA Medical School, Beijing 100853, China
[g] Departments of Otorhinolaryngology-Head and Neck Surgery, Bethune International Peace Hospital, Shijiazhuang 050081, China

ARTICLE INFO

Keywords:
Glutamate receptors
Excitability
Synaptic plasticity
Photobiomodulation
Cognition
Neuromodulation
Tinnitus

ABSTRACT

Glutamate receptors regulate neuronal excitability and drive synaptic plasticity in the auditory cortex (AC), with aberrant activation or dysfunction contributing to tinnitus pathogenesis. Photobiomodulation (PBM) exerts sustained modulatory effects on neural activity and behavioral responses across species, including humans. However, its therapeutic potential and mechanisms in noise-induced tinnitus remain unexplored. Here, we developed a noninvasive low-irradiance PBM device to target the AC of animal models, investigating near-infrared light mechanisms for reversing cortical hyperexcitability and restoring synaptic plasticity. In noise-exposed tinnitus models without significant neuronal loss, we observed abnormally elevated GluN1 activation and increased synaptic structural complexity compared to non-tinnitus or sham-exposed controls. Tinnitus models were subjected to PBM interventions with varying parameters (irradiance power: 20/40/80 mW/cm^2; exposure duration: 300/600 s). Therapeutic efficacy was validated through auditory brainstem response (ABR), gap-prepulse inhibition of acoustic startle (GPIAS), and prepulse inhibition (PPI) behavioral assays. Fluorescence

Abbreviations: PBM, photobiomodulation; CCO, cytochrome c oxidase; AC, auditory cortex; TMS, transcranial magnetic stimulation; TaVNS, transcutaneous auricular vagus nerve stimulation; CNS, central nervous system; PSD, postsynaptic densities; GluRs, glutamate receptors; MGluRs, metabotropic glutamate receptors; IGluRs, ionotropic glutamate receptors; NMDAR, N-methyl-D-aspartate receptors; AMPAR, α-amino-3-hydroxy-5-methyl-4-isoxazolepropionic acid receptors; KAR, kainate receptors; GluN, glutamate receptor, N-methyl-D-aspartate; IACUC, Institutional Animal Care and Use Committee; SPF, specific pathogen free; SPL, sound pressure level; GPIAS, gap prepulse inhibition of acoustic startle; PPI, prepulse inhibition; ABR, auditory brainstem response; IP, irradiance power; ED, exposure duration; RE, radiant exposure; IVCs, individually ventilated cages; PFA, paraformaldehyde; RT, room temperature; DAB, 3,3′-diaminobenzidine; ROI, regions of interest; SDS-PAGE, sodium dodecyl sulfate-polyacrylamide gel electrophoresis; PVDF, polyvinylidene difluoride; BSA, bovine serum albumin; TBST, Tris-buffered saline with Tween; CV, cresyl violet; DTT, dithiothreitol; TMT, tandem mass tag; SPE, solid-phase extraction; TEAB, triethylammonium bicarbonate; HPLC, high-performance liquid chromatography; IMAC, immobilized metal ion affinity chromatography; LC-MS, liquid chromatography-tandem mass spectrometry; AGC, automatic gain control; FDR, false discovery rate; TEM, transmission electron microscopy; QPCR, quantitative polymerase chain reaction; NIR, near-infrared light; IHC, immunohistochemical analyses; RSD, relative standard deviation; BP, biological processes; Log2FC, log2 fold change; CC, cellular component; E/I, excitatory-inhibitory; RAAV, recombinant adeno-associated viral vectors; TDCS, transcranial direct current stimulation; LTD, long-term depression; NO, nitric oxide; Rac1, Ras-related C3 botulinum toxin substrate 1; Map-2, microtubule-associated protein 2; PSD95, postsynaptic density protein 95; Dlgap1, discs large-associated protein 1.

* Correspondence to: No.28 Fuxing Road, Haidian District, Beijing 100853, China.
E-mail addresses: zhangzhixin0246@126.com (Z. Zhang), shm_yang@163.com (S. Yang), fangyuanwang05@163.com, 1093749813@qq.com (F. Wang).
[1] These authors contributed equally to this work.
[2] Co-author:

https://doi.org/10.1016/j.brainresbull.2025.111685

Available online 15 December 2025

microscopy of brain sections quantified c-Fos/GluN1 co-localization to image activated NMDARs, while Nissl staining assessed PBM safety across parameters. Phosphoproteomic profiling explored mechanistic pathways, with neuronal morphological changes visualized via Golgi staining and transmission electron microscopy. To confirm GluN1's pivotal role in auditory cognition, we engineered transgenic mice with GluN1 overexpression or knockdown. GluN1-overexpressing mice exhibited tinnitus-like behaviors at specific frequencies, whereas GluN1-deficient tinnitus models showed aberrant behaviors due to impaired auditory cognition. Our findings delineate noise-induced tinnitus mechanisms and PBM-mediated regulation of neuronal excitability and structural plasticity, establishing an irradiance-duration optimization framework for clinical translation.

1. Introduction

Photobiomodulation (PBM) is a noninvasive therapeutic approach that enhances mitochondrial cytochrome c oxidase activity and ATP production, while modulating membrane receptor functions and suppressing proinflammatory cytokines to regulate neural excitability (Stevens et al., 2025). These properties make PBM particularly suitable for treating central nervous system disorders involving pathological hyperexcitability in superficial brain regions like the auditory cortex (AC) (Barrett et al., 2025; Hong et al., 2025). Pathological hyperexcitability, characterized by excessive neuronal firing due to dysregulated ion channels (Karreman and Venkataramani, 2025), synaptic transmission, and intracellular signaling, represents a shared hallmark across neurological disorders (Sun et al., 2025; Korkmaz et al., 2025; Wood et al., 2025). PBM modulates this hyperexcitability through multiple mechanisms including regulation of intracellular signaling, neurotransmitter systems, and neuroinflammatory responses, offering advantages over pharmacological interventions. However, optimal PBM protocols and their precise mechanistic foundations remain inadequately characterized in most clinical contexts (Wang et al., 2025).

Subjective tinnitus involves perceiving meaningless sounds without external stimuli, with severe cases causing emotional disturbances, insomnia, and cognitive deficits (Engelke et al., 2025). This condition imposes substantial socioeconomic burdens, evidenced by the $1.2 billion spent on tinnitus-related compensation by the U.S. Department of Veterans Affairs in 2012 alone (Batts and Stankovic, 2024). Current treatments include psychotherapy, sound therapy, pharmacotherapy and physical interventions like transcranial magnetic stimulation (TMS), transcutaneous auricular vagus nerve stimulation (taVNS), yet their efficacy remains limited due to incomplete understanding of pathogenesis (Langguth et al., 2024). While multiple factors contribute to tinnitus, glutamate excitotoxicity and maladaptive synaptic plasticity appear central to its neurobiology, driving auditory pathway hyperexcitability and altered neural networks. Noise-induced tinnitus models are widely used for their fidelity in recapitulating human perceptual experiences, providing a validated paradigm for investigating subjective tinnitus mechanisms (Engineer et al., 2011).

Abnormal central nervous system (CNS) excitability and synaptic plasticity alterations involve excitotoxicity-induced hyperexcitability, which increases dendritic branching complexity and synaptic density with enlarged postsynaptic densities (Creed et al., 2021). However, excessive synaptic structural complexity can impair signal transmission, compromise plasticity, and increase neuronal energy expenditure (Yang et al., 2024). In noise-induced auditory cortical hyperexcitability, glutamatergic and GABAergic receptor dysregulation occurs, with glutamate receptors - particularly NMDARs - playing crucial roles. NMDARs are heterotetramers containing obligatory GluN1 subunits that regulate synaptic development and plasticity (Hayes et al., 2024). NMDARs are heterotetramers containing obligatory GluN1 subunits that regulate synaptic development and plasticity. Phosphorylation-mediated modulation of NMDARs controls their trafficking and synaptic efficacy, and receptor dysregulation is strongly implicated in tinnitus pathogenesis (Song et al., 2021). Thus, elucidating GluN1-dependent mechanisms underlying auditory cortical hyperexcitability and their behavioral correlations remains a key objective in NMDAR research.

Using noise-induced tinnitus models, we validated auditory cortical hyperexcitability's role in tinnitus pathogenesis and investigated PBM therapeutic parameters (exposure duration, irradiance power, radiant exposure) alongside its effects on synaptic connectivity and auditory cognition. We demonstrate that PBM downregulates hyperactivated GluN1 and rescues pathological synaptic complexity in hyperexcitable neuronal circuits. A single low-dose PBM stimulation achieved precise neuromodulation with sustained effects while preserving neurophysiological integrity. Phosphoproteomic profiling confirmed PBM acts through NMDARs and structural remodeling pathways, normalizing hyperexcitability and restoring synaptic plasticity. GluN1-overexpressing mice developed tinnitus-like behaviors, while GluN1-underexpression models showed impaired auditory processing. PBM ameliorated tinnitus-related behaviors while maintaining normal auditory acuity and hearing thresholds.

2. Materials and methods

2.1. Animals

All animals (male C57BL/6 mice, 18–24 g, 8-week-old) were housed in specific pathogen-free (SPF) conditions within a temperature-controlled sound-attenuated animal room (21 °C, background noise <30 dB) under a 12-hour light-dark cycle, with ad libitum access to food and water. All procedures were conducted in accordance with the experimental animal care and use guidelines of the Chinese PLA General Hospital (Beijing, China) and approved by its Institutional Animal Care and Use Committee (IACUC). A total of 134 mice were used in this study and no animals were excluded from the analysis. The experimental groups were distributed as follows: Control group (n = 20), Non-tinnitus group (n = 19), Tinnitus group (n = 25), PBM group (n = 26), and Sham-PBM group (n = 18). For GluN1 manipulation experiments, 13 mice were used in each group, with 7 receiving target virus injections and the remaining 6 receiving control virus injections. The required experimental animal sample size was calculated according to the resource equation method (ARIFIN et al., 2017).

2.2. Establishment of noise-induced tinnitus animal models

As in our prior work, unilateral noise exposure was selected to induce subjective tinnitus, given the critical role of preserved hearing in detecting acoustic gaps (Liu et al., 2024). Animals were anesthetized via intraperitoneal injection of tribromoethanol (125 mg/kg) and fitted with a temporary foam earplug (OHRFRIEDEN, Wehrheim, Germany) in the right ear to prevent noise-induced hearing loss. They were then placed in a sound-attenuated chamber equipped with an acoustic delivery system. A TW67 speaker (Pyramid Car Audio, Brooklyn, NY, USA), connected to an RA300 amplifier (Alesis, Cumberland, RI, USA), was positioned 10 cm from the animal's head. A 16 kHz-centered narrowband noise was delivered continuously for 1 h at 116 dB sound pressure level (SPL).

2.3. Detection of Gap and PPI Startle ratio

In tinnitus animal model studies, gap prepulse inhibition of acoustic

startle (GPIAS) and prepulse inhibition (PPI) assays were employed to assess auditory function and tinnitus induction in mice (Li et al., 2013). The GPIAS test evaluates tinnitus presence by measuring suppression of startle responses to abrupt loud sounds when preceded by silent gaps in background noise, while PPI assesses auditory detection capacity for background noise. Experiments utilized an Acoustic Startle Reflex System (SR-LAB System; San Diego Instruments, San Diego, CA). Mice were placed on a platform within a sound-attenuated chamber, with a piezoelectric transducer beneath the platform detecting pressure changes from startle responses. Startle amplitude was quantified via voltage conversion. In the "no-gap" paradigm, a 70 dB SPL narrowband noise (center frequencies: 10, 12, 16, 20, 24, and 32 kHz) was paired with a 104 dB SPL startle stimulus (20 ms). The "gap" paradigm introduced a 50-ms silent gap 130 ms before the startle stimulus. GPIAS% was calculated as the ratio of startle amplitudes between gap and no-gap trials to evaluate gap detection ability. For PPI, gaps were replaced with non-startle prepulse sounds (50 ms, 70 dB SPL), with PPI% derived from the ratio of prepulse-to-startle-only trial amplitudes (detailed formulas below) (Galazyuk and Hébert, 2015). Higher GPIAS% indicates lower tinnitus likelihood, whereas elevated PPI% reflects normative auditory processing. Mice were classified as tinnitus if they exhibited gap detection deficits at ≥ 1 background frequency among all six tested frequencies (Li et al., 2013). Following noise exposure, mice exhibiting GPIAS% decreases (>30 %) at any tested frequency were classified as tinnitus; others were designated non-tinnitus. However, GPIAS% values < 0.1 pre-noise or < -0.1 post-noise at any frequency were excluded as outliers or artifacts (Li et al., 2013). Behavioral tests were performed pre- and post-noise exposure to confirm tinnitus or hyperacusis development. Post-PBM treatment, gap startle tests were repeated at various intervals to assess tinnitus amelioration in tinnitus and stability in non-tinnitus and the control, thereby validating PBM therapeutic efficacy across treatment regimens (Turner et al., 2006; Kraus et al., 2010).

Between testing sessions, equipment was sanitized with 75 % ethanol to neutralize organic contaminants (e.g., fecal matter, odor residues). All behavioral assessments were conducted by two independent investigators blinded to group assignments to mitigate observer bias.

a. GPIAS% results were calculated using the following formula:

$$\chi\text{kHz} - \text{GPIAS\%} = \left(\frac{\text{AvgT(no} - \text{gap)} - \text{AvgT(gap)}}{\text{AvgT(no} - \text{gap)}}\right) \times 100\%$$

χ kHz-GPIAS% represents the GPIAS% at different frequencies (χ can be 10, 12, 16, 20, 24, 32). AvgT(no-gap) represents the average amplitude during no-gap trials, and AvgT(gap) represents average amplitude during gap trials.

b. PPI% results were calculated using the following formula:

$$\chi\text{kHz} - \text{PPI\%} = \left(\frac{\text{AvgT(startle)} - \text{AvgT(pre} - \text{pulse)}}{\text{AvgT(startle)}}\right) \times 100\%$$

χ kHz-PPI% represents the PPI% at different frequencies (χ can be 10, 12, 16, 20, 24, 32). AvgTstartle is the average amplitude during startle trials, and AvgTpre-pulse is the average amplitude during pre-pulse trials.

2.4. Auditory brainstem response

In tinnitus animal model studies, ABR was employed to evaluate hearing threshold shifts (Miwa et al., 2023). Mice were anesthetized via intraperitoneal injection of tribromoethanol (125 mg/kg) and positioned within a sound-attenuated chamber. Acoustic stimuli generated by a TDT RZ6 system (Tucker Davis Technologies) were delivered through an MF-1 magnetic speaker (Tucker-Davis Technologies, Alachua, FL, USA) in a closed acoustic field. Sound stimuli with 0.5 ms rise/fall times were directed into the external auditory canal. Subdermal needle electrodes (Rochester Elektro-Medical, Lutz, FL, USA) were positioned at cranial sites to record ABR signals. Responses were averaged 512 times and bandpass-filtered (100–3000 Hz). Stimulus intensity began at 90 dB SPL, decreasing in 10 dB SPL steps, with test frequencies spanning 10, 12, 16, 20, 24, and 32 kHz. ABR thresholds were defined as the lowest intensity eliciting reproducible wave II at each frequency (Kim et al., 2025). Tests were conducted pre-noise exposure, post-noise exposure, and post-PBM on the left ear to assess hearing threshold dynamics. Right ear testing was omitted, as our prior work confirmed preserved hearing in the foam-protected right ear under these noise conditions (Liu et al., 2024).

Table 1
Specifications for laser parameters.

Irradiation parameters	
Central wavelength (nm)	830
Wavelength tolerance (nm)	± 5
Max output power (W)	1
Fiber core diameter (μm)	105
Mode	Continuous wave mode
Beam shape	Circular
Adjustable range of spot (cm)	0.5–5.0
Treatment parameters	
Irradiance power at skin/skull (mW/cm^2)	20/40/80
Laser transmission ratio to skin and skull (%)	22.67
Laser transmission ratio to skull (%)	59.33
Distance to the head from the end of a fiber (cm)	4
Exposure duration (s)	300/600
Focused beam spot size (mm^2)	12.56
Number of points irradiated	1
Radiant exposure at brain (J/cm^2)	12/24

2.5. PBM plan screening experiment

A VCL-830nmM1 low-irradiance laser device (Beijing Honglan Optoelectronics, China) was used for PBM. Animals were assigned to four PBM treatment regimens (Plan A/B/C/D) based on differential parameter combinations of irradiance power (IP), exposure duration (ED), and radiant exposure (RE). Detailed parameters are provided in Table 1, with the experimental timeline shown in OFig. 2A. The parameter design was based on the study by Namgue Hong et al. (2023) Specific regimens included:Plan A: IP = 40 mW/cm^2, ED = 600 s; Plan B: IP = 40 mW/cm^2, ED = 300 s; Plan C: IP = 20 mW/cm^2, ED = 600 s; Plan D: IP = 80 mW/cm^2, ED = 300 s.

The rationale for this design is as follows:

- IP-controlled comparison: Plans A vs. B share identical IP (40 mW/cm^2) but differ in ED (600 vs. 300 s), isolating ED-dependent PBM effects.
- ED-controlled comparison: Plans A vs. C (ED = 600 s) and Plans B vs. D (ED = 300 s) maintain fixed ED with varying IP (40 vs. 20 mW/cm^2; 40 vs. 80 mW/cm^2), enabling IP efficacy analysis.
- RE-controlled comparison: Plans A vs. D (RE = 24 J/cm^2) and Plans B vs. C (RE = 12 J/cm^2) match total energy delivery (RE = IP × ED) to assess IP/ED trade-offs.

2.6. PBM Irradiance power measurement

To prepare murine temporal skull fragments, mice were first deeply anesthetized via intraperitoneal injection of tribromoethanol (125 mg/kg) to ensure pain-free immobilization during surgery. Following successful anesthesia, the mouse was secured on a surgical platform in a supine position. Sterile surgical instruments were used to excise dome-shaped skull fragments (~1 ×1 cm) along the temporal region. Fragments were categorized as hairy or hair-free skull fragments based on retained/removed adherent hair. For hair removal, forceps were employed to meticulously remove adhering hair without compromising structural integrity. Harvested fragments were immediately placed in Petri dishes and rinsed with physiological saline to eliminate residual

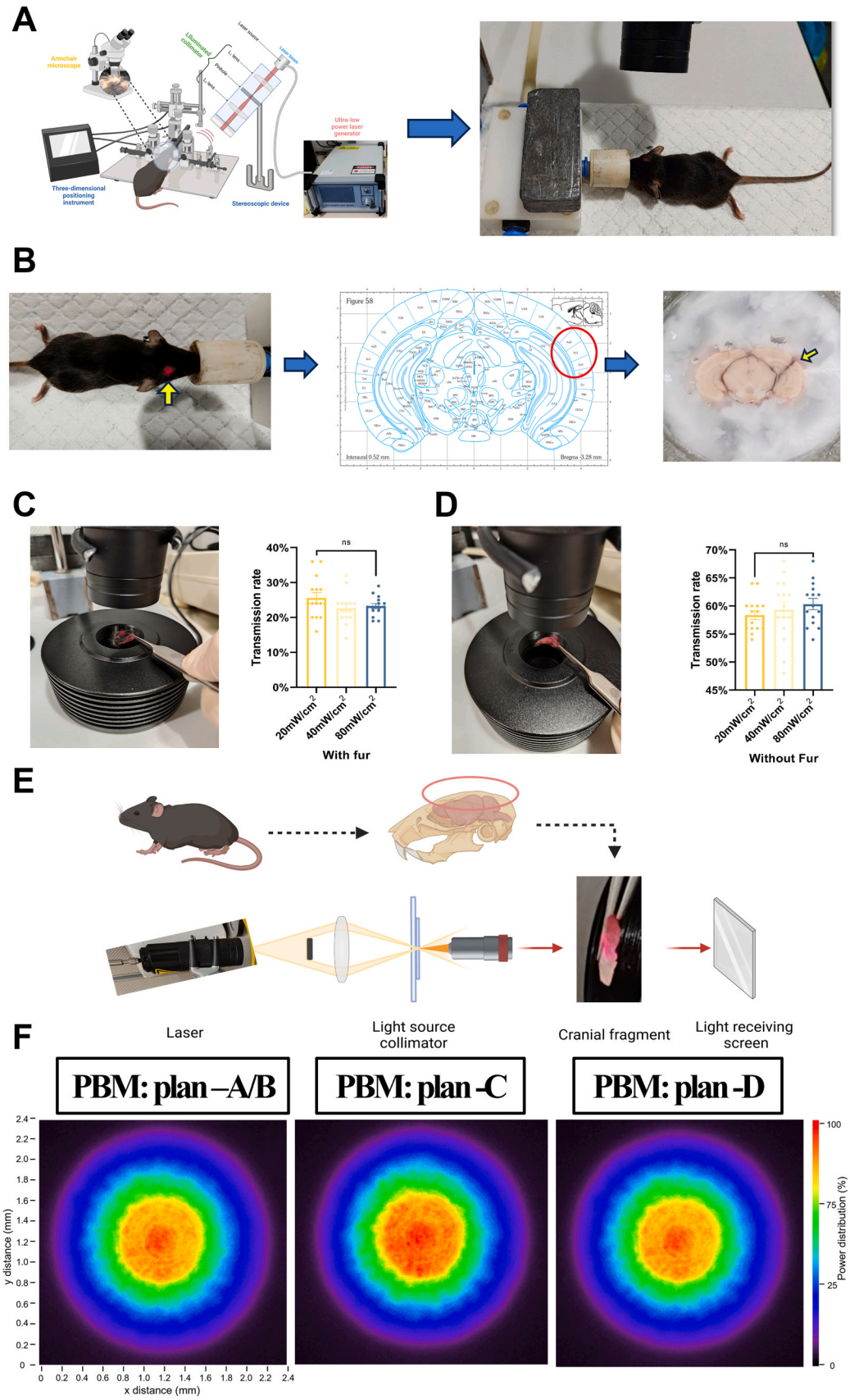

Fig. 1. A Stereotaxic targeting of the C57 mouse AC for PBM (830 nm NIR) to modulate neuronal excitability. B Ex vivo validation of light targeting accuracy to the AC via stereotaxic-guided ablation (yellow arrow indicates illumination area). C Transmittance of NIR through skull fragments with fur measured by laser power meter (n = 15). D Transmittance of NIR through skull fragments without fur (n = 15). E Schematic of energy distribution profiling for transcranial PBM under different regimens. F Visualized energy distribution patterns post-transcranial PBM (n = 6). ns denotes $P > 0.05$; error bars represent SEM.

hair or blood. Subsequently, fragments were transferred to a JC-C30 laboratory dryer (Qingdao Juchuang Century, China) and dried at 30°C for 10 min to remove residual moisture. All fragments were freshly prepared before each experiment to simulate near-infrared light penetration through the skull and its subsequent cerebral effects.

A VCL-CLT-01C laser power meter (Beijing Honglan Optoelectronics, China) was employed to measure PBM transmission through intact or hair-free skull fragments under different treatment regimens. The laser power meter was preheated for 30 min to stabilize performance. The laser was then activated, and the optical path was aligned using a 620 nm aiming beam to ensure precise irradiation onto the power meter display, with the light source aperture positioned 4 cm from the detector. The laser was temporarily deactivated for zero-point calibration to eliminate background noise. Skull fragments (with or without adherent hair) were sequentially placed in the optical path. Laser IP was set to 20, 40, or 80 mW/cm^2, and stabilized power readings were recorded. Transmittance (%) was calculated as Measured Power/Set Power-$\times$ 100 %. This protocol evaluated PBM penetration efficiency through hairy versus hair-free skull preparations and its dependence on IP.

2.7. PBM spot energy distribution detection

A CN0204VIS beam profiler (Changchun Xinchan Industry, China) was utilized to characterize energy attenuation profiles of PBM regimens transmitted through murine skull fragments. Standardized murine skull fragments (prepared as previously described) were positioned in the optical path. The beam profiler probe was maintained 5 mm from the skull fragment using a three-dimensional adjustment stage, with the collimating lens positioned 4 cm from the probe. Prior to each measurement, the system was calibrated with a NIST-traceable calibration light source. Sampling frequency was set to 10 Hz, and exposure time was auto-optimized to 70 % full-scale. Transmitted beam energy distribution was quantified and imaged using Lasescope NX software (v1.8, Changchun Xinchan Industry, China). Ambient temperature was strictly controlled at 21 $\pm$ 1°C throughout experiments to minimize thermal drift artifacts.

2.8. PBM irradiation

Mice were initially anesthetized with 2 % isoflurane (carrier gas: 95 % O_2/5 % CO_2) and maintained under 1–1.5 % isoflurane via a nose cone using an R540 anesthesia machine (RWD, China). Core body temperature was stabilized at 37.0 $\pm$ 0.5°C with a ThermoStar thermoregulation system (RWD, China). Cranial hair was removed with hair and temporal muscle, followed by immobilization in a 68017 dual-arm stereotaxic frame (RWD, China). Ophthalmic erythromycin ointment was applied to protect corneas. The surgical field was disinfected with alternating iodine and ethanol scrubs (3 cycles). An 8-mm sagittal scalp incision was made, and subcutaneous tissue was bluntly dissected to expose the skull surface. Under microscopic guidance, a stereotaxically mounted microinjection needle was positioned at coordinates (ML: −4.2 mm, AP: ±2.96 mm, DV: −2.25 mm) (Yao et al., 2019). A collimator-equipped secondary manipulator arm (beam diameter: 2 mm, divergence angle <0.5 mrad) delivered continuous-wave laser irradiation 4 cm from the target site. The incident angle was calibrated to 55 $\pm$ 5° (perpendicular to the temporal bone plane) using a digital goniometer, confining illumination to a 1 mm-radius circular area. Mice received 830 nm PBM for 300 or 600 s (treatment parameters detailed in Section 2.5). Post-PBM, the scalp incision was closed with 4.0 mm absorbable sutures (Nantong Walcon, China). Bacitracin ointment was applied to prevent infection, and animals recovered in pre-warmed individually ventilated cages (IVCs). The above procedure was performed 3 h after the mice were confirmed to have tinnitus. No procedural mortality or morbidity occurred in this study. Based on our findings that a single PBM session resulted in improvements in tinnitus-like behavior starting from day 2, with therapeutic effects lasting for at least 6 days, we opted to administer only one PBM treatment in the present experiment.

To further validate that laser irradiation could precisely target the right auditory cortex, we inserted a 2.5 mL syringe along the extended trajectory connecting the guidance point and the light source, and injected an appropriate amount of methylene blue as a tracer. This procedure allowed us to determine whether the laser emitted from the light source covered the target brain region after passing through the selected guidance point (Fig. 1B).

2.9. Immunocytochemistry

Mice were anesthetized with 1 % pentobarbital sodium and transcardially perfused with physiological saline followed by 4 % paraformaldehyde (PFA). Brains (including AC) were carefully extracted and post-fixed in 4 % PFA overnight. Tissues were subsequently dehydrated in 20 % and 30 % sucrose solutions for 3 days each. Coronal sections (30 μm thickness) were obtained using a Leica CM1860 cryostat (Germany). For immunofluorescence staining, sections were pre-blocked with 5 % donkey serum and 0.3 % Triton X-100 at room temperature (RT) for 2 h, followed by incubation with primary antibodies at 4°C for 12 h: rabbit anti-GluN1 (1:500, GeneTeX, GTX133097) and guinea pig anti-c-Fos (1:500, Synaptic Systems, 226308). Sections were then incubated with secondary antibodies—goat anti-rabbit 647 (1:500, Servicebio, GB23303) and donkey anti-guinea pig 594 (1:500, Yeasen, 34512ES60)—at RT for 2 h. For 3,3′-diaminobenzidine (DAB) immunohistochemistry, brain sections were pretreated with 3 % H2O2 in PBS to quench endogenous peroxidase activity, dehydrated in graded ethanol series, and mounted with neutral balsam. All images were acquired using a virtual slide microscope (SV120, Olympus, Japan) or laser scanning confocal microscope (LSM780, Zeiss, Germany). Double immunofluorescence co-labeling for c-Fos and GluN1 was performed in six groups: Control, Non-tinnitus, Tinnitus, Control+PBM, Non-tin+PBM, and Tinnitus+PBM. Three equally sized regions of interest (ROIs) were randomly selected within the right AC of each section. Neurons fully contained within ROIs and not intersecting exclusion boundaries were counted. ImageJ software (version 1.52a, National Institutes of Health, Bethesda, MD, USA) was used for quantitative analysis.

2.10. Western blot analysis

Proteins were extracted from right AC tissues using RIPA buffer (ThermoFisher) supplemented with protease and phosphatase inhibitor cocktails (ThermoFisher). Following centrifugation (13,000 rpm, 15 min, 4°C), supernatants were collected into fresh 1.5 mL tubes and stored at −80°C. Total protein (15–30 μg) was resolved on 10–15 % sodium dodecyl sulfate-polyacrylamide gel electrophoresis (SDS-PAGE) gels and electrophoretically transferred to polyvinylidene difluoride (PVDF) membranes (Bio-Rad) using transfer buffer. Membranes were blocked with 5 % bovine serum albumin (BSA) in Tris-buffered saline with Tween 20 (TBST; 10 mM Tris-HCl pH 7.4, 150 mM NaCl, 0.1 % Tween 20) and incubated with appropriate primary and secondary antibodies. GluN1 was detected using anti-GluN1 antibody (1:1000, GeneTeX, GTX133097). GAPDH (1:5000, Servicebio , GB15004) served as the loading control. Protein bands were visualized using Clarity™ Western ECL Substrate (Bio-Rad) and imaged with Image Lab 6.0.1 (Bio-Rad). Densitometric analysis was performed by normalizing target protein band intensities to GAPDH and expressed as fold changes relative to controls.

2.11. Nissl staining analysis

Mice were anesthetized with 1 % pentobarbital sodium and transcardially perfused with cold saline using a perfusion pump, followed by decapitation. Brains were extracted and fixed in 4 % PFA in 0.1 M

phosphate buffer (pH 7.4) for ≥ 48 h. Tissues were then dehydrated in 20 % and 30 % sucrose solutions for 3 d each. Coronal sections (20 μm thickness) of the AC were obtained using a Leica CM1860 cryostat (Germany). Prior to use, tissues were mounted on gelatin-coated slides overnight. After dehydration in graded alcohol series, auditory cortex sections were stained with pre-warmed 0.3 % cresyl violet (CV) solution for 20 min at RT. Following destaining with 95 % ethanol containing 0.3 % glacial acetic acid, sections were dehydrated in 100 % ethanol and 100 % xylene, then mounted with DPX. Unbiased cell counting was performed in six experimental groups: Control, Non-tinnitus, Tinnitus, Control+PBM, Non-tin+PBM, and Tinnitus+PBM. Three 250 μm × 250 μm square ROIs were randomly selected in the right auditory cortex. Only cells exhibiting Nissl-stained cytoplasm with intact nuclei fully contained within the section were counted. Cells partially or completely within ROIs and not intersecting exclusion lines were included. Quantitative analysis was conducted using ImageJ software.

2.12. Tissue isolation and sample preparation from AC for mass spectrometry analysis

Mice from the Control, Tinnitus, and PBM-treated (4 days after PBM treatment) groups were euthanized under anesthesia, and right auditory cortex tissues were harvested. For each group, brain specimens from 6 mice were pooled pairwise to generate 3 samples for LC-MS/MS analysis. Tissue proteins were extracted using lysis buffer (8 M urea, 1 % Triton X-100, 65 mM dithiothreitol (DTT), 1 % protease inhibitor cocktail, PR619) for subsequent analyses. Peptides were purified with reversed-phase Sep-Pak C18 cartridges and eluted with 50 % acetonitrile. A 1 % aliquot of eluted peptides was subjected to proteomic profiling. Protein content was validated through SDS-PAGE and Coomassie blue staining.

2.13. Digestion, fractionation, and affinity enrichment

Each tissue protein sample was subjected to three cycles of high-intensity ultrasonication on ice using an ultrasonic processor (Scientz), followed by tandem mass tag (TMT) labeling. Digested peptides were desalted with Strata X C18 solid-phase extraction (SPE) columns (Phenomenex) and vacuum-dried. Samples were reconstituted in 0.5 M triethylammonium bicarbonate (TEAB) and processed using a sixplex TMT kit per manufacturer's instructions. Peptides were fractionated via high-pH reversed-phase high-performance liquid chromatography (HPLC) on an Agilent 300 Extend C18 column (5 μm particles, 4.6 mm inner diameter, 250 mm length). Separation was performed with a 60-min gradient from 8 % to 32 % acetonitrile in 10 mM ammonium bicarbonate (pH 9), yielding 60 fractions that were pooled into six final fractions. Finally, phosphopeptides were enriched by incubating peptide mixtures with agitated immobilized metal ion affinity chromatography (IMAC) microsphere suspensions for subsequent liquid chromatography-tandem mass spectrometry (LC-MS/MS) analysis.

2.14. LC-MS/MS analysis

Phosphorylation sites were identified using a Thermo Scientific™ Q Exactive™ Plus mass spectrometer. Intact peptides were measured in the Orbitrap analyzer at a resolution of 60,000. The spray voltage was set to 2.3 kV, with automatic gain control (AGC) employed to prevent ion trap overfilling. For MS scans, the mass-to-charge ratio (m/z) range was 400–1200, and the first fixed mass was set to 110 m/z. The DIA data in this experiment were analyzed using the Spectronaut (v18) search engine with default parameters. The database used was Mus_musculus_10090_SP_20231220.fasta (17,191 sequences) with Trypsin/P digestion and up to 2 missed cleavages allowed. Carbamidomethyl (C) was set as fixed modification, while variable modifications included methionine oxidation, protein N-terminal acetylation, and phosphorylation of serine, threonine, and tyrosine. A decoy database was incorporated to calculate the false discovery rate (FDR), with the FDR threshold set at 1 % for protein, peptide, and modification site identification.

2.15. Bioinformatics analysis

Identified proteins were functionally annotated against Gene Ontology (GO; http://www.geneontology.org), Kyoto Encyclopedia of Genes and Genomes (KEGG; http://www.genome.jp/kegg/pathway.html), Clusters of Orthologous Groups (COG; http://www.ncbi.nlm.nih.gov/COG/), and evolutionary genealogy of genes: Non-supervised Orthologous Groups (eggNOG; http://eggnogdb.embl.de/). GO and KEGG analyses were employed to evaluate the enrichment of differentially expressed proteins against all identified proteins. GO annotations were categorized into three major classifications: Biological Process, Cellular Component, and Molecular Function. Fisher's exact test was applied to assess the significance of GO enrichment for differentially expressed modified proteins (using all identified proteins as background), with a P value < 0.05 considered statistically significant. The KEGG PATHWAY database was utilized for pathway enrichment analysis of differentially expressed modified proteins. Fisher's exact test was also used to determine the significance of pathway enrichment (with all identified proteins as background), adopting the same significance threshold (P value < 0.05). For KEGG pathway annotation, identified proteins were subjected to BLASTP analysis (e-value ≤ 1e-4), and the highest-scoring alignment result was selected for annotation.

2.16. Transmission Electron Microscopy (TEM)

Right AC tissues were fixed in 2.5 % glutaraldehyde, washed thrice in phosphate-buffered saline (PBS; pH 7.2), post-fixed in 1 % osmium tetroxide, dehydrated through graded ethanol and acetone series, and embedded in epoxy resin. Ultrathin sections (65 nm) were prepared using an RMC MT-XL ultramicrotome, collected on 100-mesh copper grids, and imaged at 80 kV using a JEOL TEM (Japan). Three samples were analyzed per group. For each sample, three random fields of view were captured at low magnification (×16,000, scale bar = 1 μm) and high magnification (×30,000, scale bar = 500 nm). The synaptic ultrastructural features visible in these micrographs—including synaptic density, synaptic curvature, postsynaptic density (PSD) thickness, PSD area, synaptic cleft width, and active zone length—were quantified for statistical analysis.

2.17. Golgi Staining

Right AC tissues were dissected from mice deeply anesthetized with tribromoethanol (125 mg/kg) and immersed in Golgi-Cox solution (FD NeuroTechnologies, PK401, Columbia, MD). After 24 h, the immersion solution was refreshed. Impregnated tissues were frozen in molten isopentane and cryosectioned at 180 μm. Sections were air-dried overnight at 24°C, developed (FD NeuroTechnologies), dehydrated in ethanol and xylene, and coverslipped. Pyramidal neurons in the AC were imaged using an Olympus BX530 light microscope (Tokyo, Japan). Image analysis was performed with ImageJ. For each group, three sections per mouse and one image per section were analyzed.

2.18. Stereotactic injection

AC localization followed our previously described PBM targeting protocol. A 10 μl microsyringe (RWD, R-480, China) was used to inject 250 nl of either the experimental virus (rAAV-hsyn-Grin1-EGFP-WPREs) or control virus (PFD-rAAV-hSyn-EGFP-WPRE-hGH polyA) into the right AC at 50 nl/min. This protocol aimed to assess whether GluN1 overexpression in naïve mice induces tinnitus-like behaviors. Similarly, the experimental virus (rAAV-hsyn-EGFP-5'miR-30a-shRNA(Grin1)-3'-miR30a-WPREs) or control virus (PFD-rAAV-hSyn-EGFP-5'miR-30a-

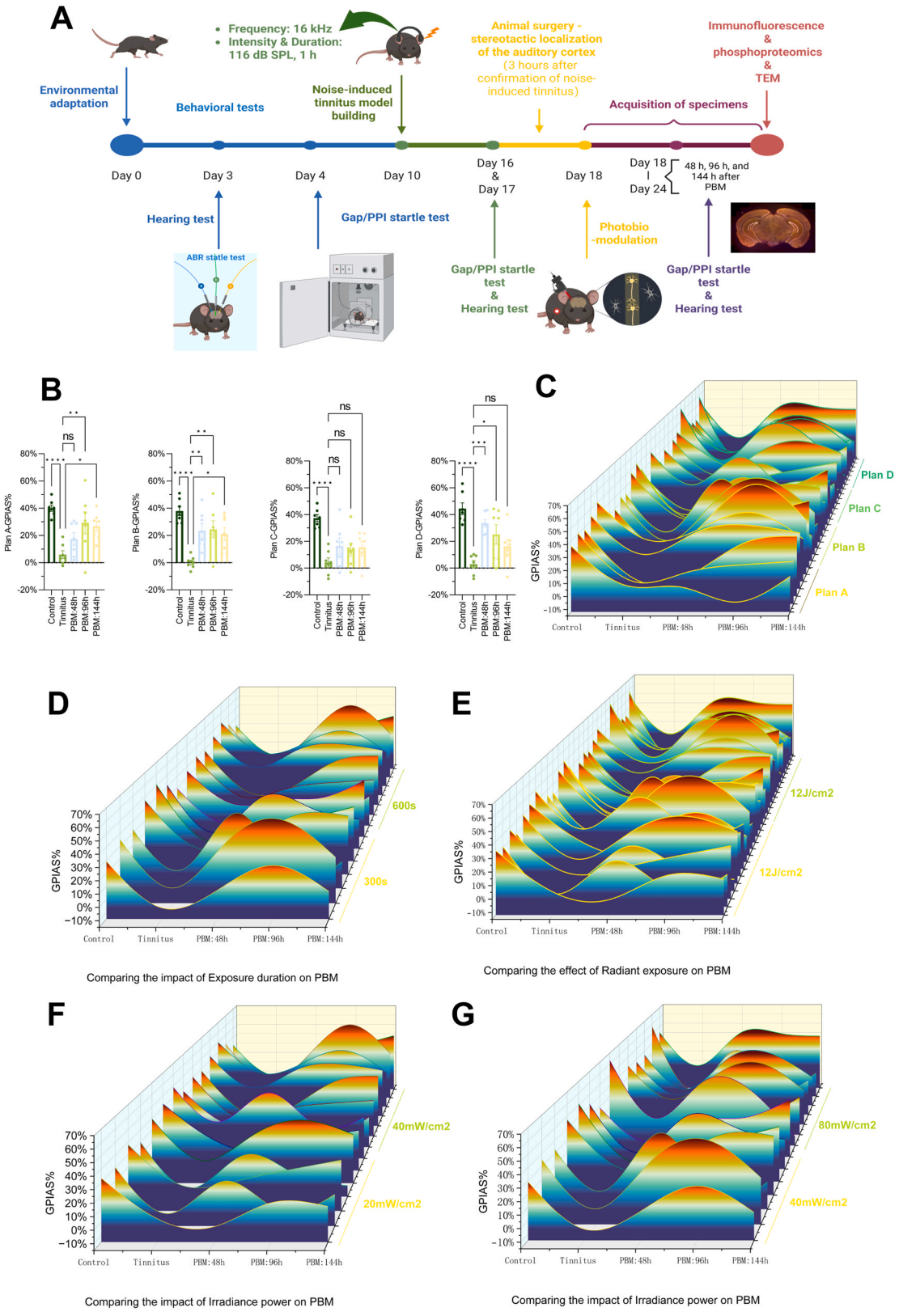

Fig. 2. A Experimental timeline: Mice underwent 3-day habituation, baseline ABR, GPIAS, and PPI testing. Noise exposure (116 dB, 16 kHz, 60 min) was delivered to the left ear on day 10. Post-noise GPIAS/PPI screening on day 17 classified mice into Tinnitus and Non-tinnitus groups. Tinnitus mice received PBM under four regimens (A/B/C/D) to determine optimal parameters. Brain samples were collected at 12/24/48/96/144 h post-PBM. B Comparative therapeutic efficacy of Plans A/B/C/D in tinnitus mice (n = 20). C-G 3D waterfall plots illustrating parameter-specific therapeutic effects: C: Tinnitus frequency distribution under Plans A/B/C/D (n = 20); D: Impact of ED on efficacy (n = 10); E: Comparison under identical total RE (n = 20); F,G: IP-dependent effects (n = 10). Color gradient: Increasing red intensity corresponds to higher gap startle test scores (reduced tinnitus likelihood).

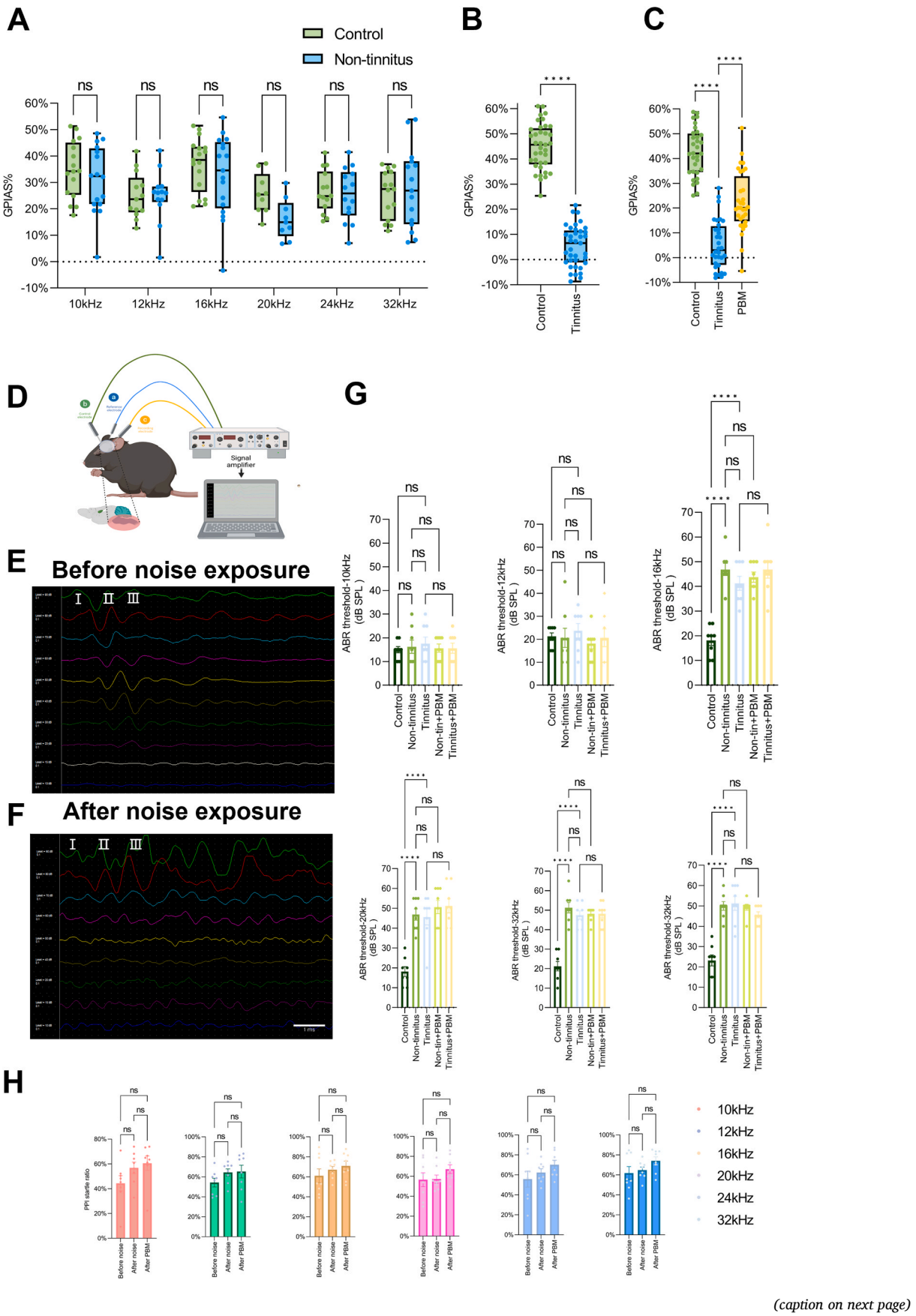

(caption on next page)

Fig. 3. A GPIAS% comparison in Non-tinnitus mice (excluding those allocated to immunofluorescence or genetic editing) pre- and post-noise exposure across 10/12/16/20/24/32 kHz frequencies ($n = 19$). B GPIAS% comparison in Tinnitus mice (excluding immunofluorescence/genetic editing cohorts) pre- and post-noise exposure ($n = 25$). C GPIAS% in PBM-treated Tinnitus mice (excluding immunofluorescence/genetic editing cohorts) at day 4 post-treatment ($n = 26$). D Schematic of the ABR experimental paradigm. E, F ABR threshold curves in C57 mice pre-noise (E) and post-noise (F) exposure. G ABR thresholds across frequencies (10, 12, 16, 20, 24, 32 kHz) for Control, Non-tinnitus, Tinnitus, Non-tin+PBM, and Tinnitus+PBM groups ($n = 40$). H PPI startle ratios in Tinnitus mice ($n = 8$).

shRNA(scramble)-3′-miR30a-WPREs) was injected into the right AC to model PBM-induced GluN1 downregulation in tinnitus mice and evaluate behavioral recovery. The microsyringe remained in situ for 10 min post-injection to prevent reflux. Viral-injected mice underwent behavioral testing, Western blot, and quantitative polymerase chain reaction (qPCR) 4 weeks post-injection. Adeno-associated virus serotype 2/9 (AAV2/9) vectors were packaged and provided by BrainVTA (Wuhan, China).

2.19. Quantitative real-time polymerase chain reaction

Total RNA was isolated using TRIzol™ Reagent (Invitrogen, Carlsbad, CA, USA) and reverse-transcribed into cDNA with a PrimeScript™ RT Kit (RR037, TaKaRa, China). qPCR was performed on a StepOnePlus™ Real-Time PCR System (272001262, Applied Biosystems, China) using SYBR Green Master Mix. Reaction mixtures contained 10 μl SYBR Green PCR premix, 7 μl diethyl pyrocarbonate (DEPC)-treated H2O, 2 μl forward/reverse primers, and 1 μl cDNA. Primer sequences were:

- GluN1: Forward 5′-GTTTGACCCAGGAACCAAGAATG-3′, Reverse 5′-CGTTGATTAGCTGAAGTCCGATG-3′
- GAPDH: Forward 5′-CCTCGTCCCGTAGACAAAATG-3′, Reverse 5′-TGAGGTCAATGAAGGGGTCGT-3′

2.20. Statistical analysis

Data are presented as the mean ± standard error of the mean (SEM). After assessing normality using the Shapiro-Wilk test, statistical comparisons were performed using paired-sample *t*-tests or one-way analysis of variance (ANOVA) followed by Bonferroni's post hoc test, as appropriate. Specifically, comparisons across three or more groups (e.g., Control, Non-tinnitus, Tinnitus) were performed using one-way ANOVA, while paired *t*-tests were applied for before-and-after comparisons in the gene-edited mouse experiments. All analyses were conducted using GraphPad Prism 9.5.0 (GraphPad Software, San Diego, CA, USA), and a P-value < 0.05 was considered statistically significant.

3. Results

3.1. Low-intensity PBM penetrates the skull to modulate central neural activity with unaltered post-cranial optical properties across IP variations

PBM exerts biological effects by modulating mitochondrial energy synthesis, suppressing cellular peroxidation, or regulating membrane receptor functions, with demonstrated therapeutic efficacy in Alzheimer's disease, Parkinson's disease, and epilepsy. We developed a novel PBM platform capable of precise spatiotemporal modulation (0.5–5 mm range) targeting single or multiple brain regions. In compliance with Safety of Laser Products - Part 1: Equipment Classification and Requirements (IEC 60825–1), near-infrared light (NIR) IP was maintained below 100 mW/cm^2, ensuring biosafety (Chen and Hadi, 2021). Fig. 1B illustrates stereotaxic localization of the right AC in C57 mice based on the Paxinos & Franklin mouse brain atlas (2019), confirming precise light targeting to the AC with minimal off-target effects on adjacent regions (Xiong et al., 2015). To evaluate transcranial NIR penetration, we prepared two skull fragment groups: with fur and without fur. Both groups received circular illumination (1 mm radius) at IPs of 20, 40, and 80 mW/cm^2. As shown in Fig. 1C, transmittance (%) through skull fragments with fur showed no significant differences across IPs (20 mW/cm^2: 25.60 ± 1.50 %; 40 mW/cm^2: 22.67 ± 1.13 %; 80 mW/cm^2: 23.27 ± 0.72 %; $F(2, 42) = 1.776$, $P = 0.182$, n = 15). Similarly, hair-free skull fragments exhibited comparable transmittance (20 mW/cm^2: 58.40 ± 0.79 %; 40 mW/cm^2: 59.33 ± 1.15 %; 80 mW/cm^2: 60.33 ± 0.99 %; $F(2, 42) = 0.753$, $P = 0.4773$, n = 15). However, in Fig. 1D, transmittance through skulls fragments without fur was significantly higher than through skulls fragments with fur at all IPs (****$P < 0.0001$, n = 15), prompting subsequent in vivo PBM delivery via direct skull exposure to maximize energy delivery. Beam profiler analysis (Fig. 1E) revealed no significant energy loss or heterogeneous distribution across IPs (20, 40, and 80 mW/cm^2), confirming negligible refractive scattering through murine skulls.

3.2. PBM at 40 mW/cm^2 alleviates tinnitus without compromising auditory thresholds or information processing in mice

Having established the feasibility of low-irradiance transcranial PBM in mice with no significant intergroup differences in vitro, we next investigated whether PBM modulates hearing thresholds or tinnitus-like behaviors in sham noise-exposed controls, noise-exposed non-tinnitus mice, and noise-induced tinnitus models. Tinnitus mice were subjected to PBM under four regimens (Plan A/B/C/D), and therapeutic outcomes were evaluated via gap startle test to assess tinnitus persistence and behavioral improvement (Fig. 2B). In Plans A, B, and D, GPIAS% progressively increased across tinnitus frequencies from post-treatment day 2 onward [Plan A: Control: 40.07 ± 2.27 %; Tinnitus: 5.93 ± 2.85 %; PBM:48 h: 17.43 ± 4.62 %; PBM:96 h: 29.37 ± 8.04 %; PBM:144 h: 26.75 ± 3.80 %, $F(4, 30) = 7.298$, $P = 0.0003$, n = 5; Plan B: Control: 37.93 ± 3.30 %; Tinnitus: 0.09 ± 1.71 %; PBM:48 h: 23.39 ± 5.34 %; PBM:96 h: 24.57 ± 6.17 %; PBM:144 h: 21.06 ± 4.97 %, $F(4, 30) = 8.822$, $P < 0.0001$, n = 5; Plan D: Control: 44.41 ± 4.34 %; Tinnitus: 2.95 ± 2.78 %; PBM:48 h: 33.47 ± 2.77 %; PBM:96 h: 25.21 ± 7.34 %; PBM:144 h: 16.25 ± 5.28 %, $F(4, 30) = 10.88$, $P < 0.0001$, n = 5]. However, Plan C exhibited an upward trend without achieving statistical significance at any timepoint [Plan C: Control: 37.35 ± 2.60 %; Tinnitus: 4.22 ± 3.45 %; PBM:48 h: 16.42 ± 6.03 %; PBM:96 h: 13.84 ± 4.94 %; PBM:144 h: 15.64 ± 4.32 %, $F(4, 30) = 7.488$, $P = 0.0003$, n = 5]. The elevated GPIAS% in PBM-treated tinnitus mice indicates neuromodulatory effects of PBM on AC circuits (Fig. 2C). Both Plan B (lower IP) and Plan D demonstrated comparable therapeutic efficacy from day 2, with Plan B selected for subsequent studies due to superior biosafety profile.

To dissect the differential impacts of ED, IP, and RE on therapeutic outcomes, 3D waterfall plots were generated (Fig. 2D-G). Despite identical IP, prolonged ED did not enhance efficacy, as even short ED achieved comparable therapeutic effects (Fig. 2D). Divergent outcomes under identical RE (Fig. 2E) suggest that total RE delivered to the AC is not the sole determinant of PBM's biological effects. Notably, at matched ED, PBM at 20 mW/cm^2 failed to improve tinnitus-like behaviors over the 6-day observation window, whereas PBM at 40, 80 mW/cm^2 significantly reduced symptoms from day 2 (Fig. 2F, G), indicating a critical IP threshold for neural modulation.

We further explored whether PBM induces neuromodulatory effects in Control and Non-tinnitus groups. Supplementary Figure 1 A demonstrates that Control mice exhibited no tinnitus-like behaviors across 10–32 kHz frequencies during the 6-day PBM observation window. Similarly, Non-tinnitus mice showed no behavioral changes under PBM at any tested frequency (Supplementary Figure 1B). Collectively, these findings confirm that tinnitus mice receiving PBM at 40 mW/cm^2 for

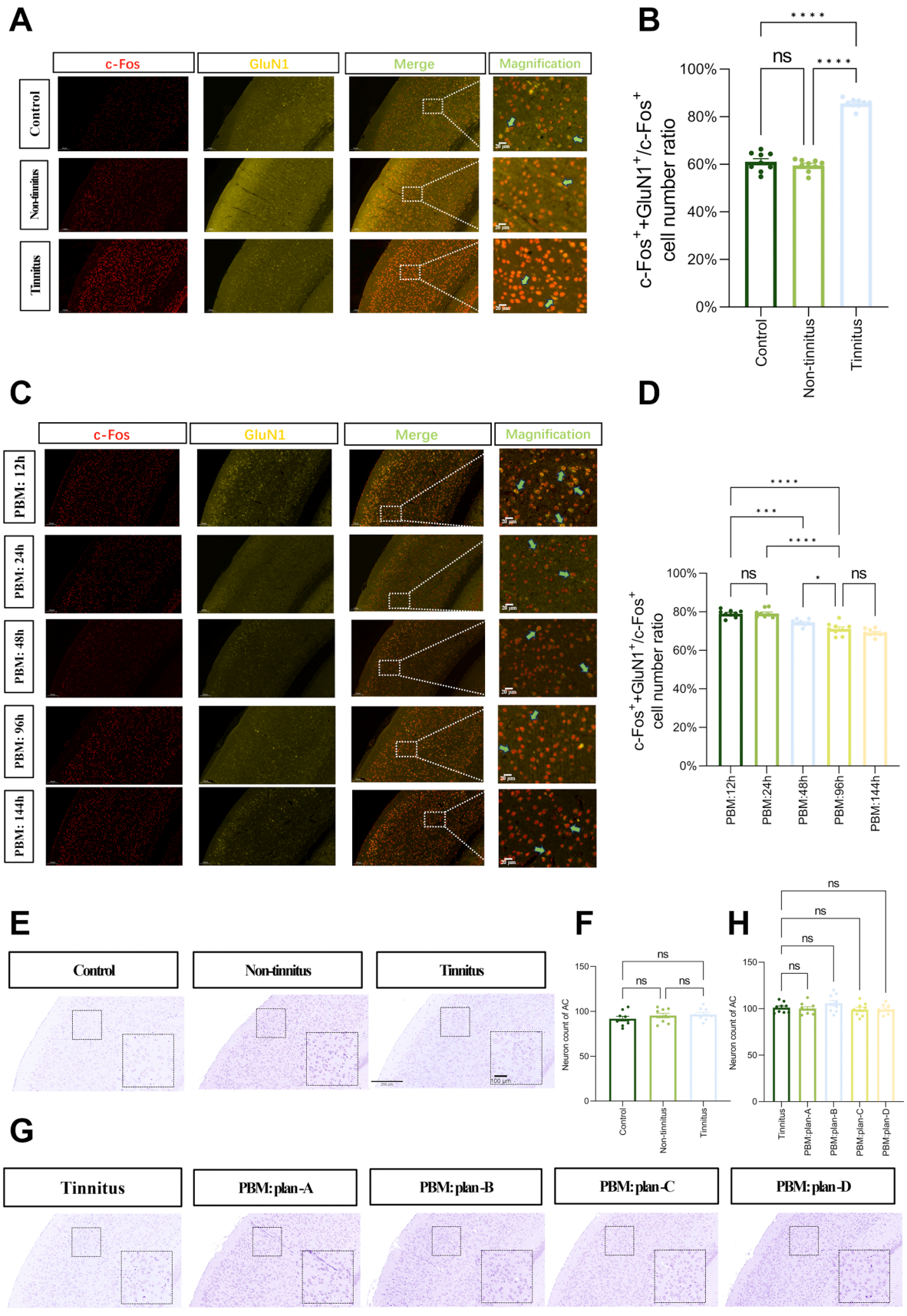

(caption on next page)

Fig. 4. A Representative coronal brain sections of AC showing c-Fos/GluN1 co-expression staining pre-treatment. From top: sham noise-exposed control, noise-exposed non-tinnitus, and noise-exposed tinnitus mice. Tinnitus mice exhibited significantly elevated GluN1 activation compared to control and non-tinnitus groups. Right panels: high-magnification views of AC. Scale bars: 250 μm (low) and 10 μm (high). B Quantitative analysis of c-Fos/GluN1 co-expression in AC across control, non-tinnitus, and tinnitus groups (n = 9). C Representative coronal sections of AC showing c-Fos/GluN1 co-expression at 12, 24, 48, 96, and 144 h post-PBM in tinnitus mice. Mid-to-high dose 830 nm PBM effectively reversed AC hyperexcitability. Right panels: high-magnification views. Scale bars: 250 μm (low) and 10 μm (high). D Quantitative analysis of c-Fos/GluN1 co-expression in AC across PBM timepoints (n = 15). E Representative Nissl-stained AC sections showing viable neurons in control, non-tinnitus, and tinnitus groups. Scale bars: 250 μm (low) and 10 μm (high). F Quantification of Nissl-positive neurons in AC across groups (n = 9). G Nissl-stained AC sections from tinnitus mice and those treated with PBM protocols (Plan-A to Plan-D). Scale bars: 250 μm (low) and 100 μm (high). H Quantification of Nissl-positive neurons in AC across treatment groups (n = 12). Statistical annotations: ns ($P > 0.05$); *$P < 0.05$; **$P < 0.01$; ***$P < 0.001$; ****$P < 0.0001$. Error bars represent SEM.

300 s derive significant therapeutic benefits without adverse effects on Control or Non-tinnitus cohorts.

We evaluated tinnitus-like behaviors in Non-tinnitus, Tinnitus, and PBM-treated mice (830 nm, 40 mW/cm^2, 300 s) via GPIAS on day 4 post-treatment. Across all frequencies, Non-tinnitus mice exhibited no GPIAS% changes pre- vs. post-noise exposure ($P = 0.4415 > 0.05$; Fig. 3A). Tinnitus mice showed significant GPIAS% reductions (44.95 ± 1.48 % vs. 5.36 ± 1.33 %, ****$P < 0.0001$; Fig. 3B), confirming successful tinnitus induction. PBM-treated tinnitus mice demonstrated marked GPIAS% recovery (42.67 ± 1.70 % vs. 5.22 ± 1.75 % vs. 22.32 ± 2.12 %, ****$P < 0.0001$; Fig. 3C). Among all tinnitus mice not allocated to immunofluorescence or genetic editing, 25 were assigned to the Tinnitus group and 26 to the PBM group for phosphoproteomics, WB, TEM, and Golgi staining. PBM improved tinnitus-like behaviors in 21/26 mice (80.77 %) and 26/32 tinnitus frequencies (81.25 %), indicating PBM as a potential therapeutic strategy for tinnitus.

ABR testing revealed no significant improvements in hearing thresholds following PBM treatment (Fig. 3D-G). At 16 kHz, Control mice exhibited thresholds of 18.13 ± 2.10 dB, whereas Non-tinnitus and Tinnitus groups showed elevated thresholds of 46.88 ± 2.49 dB and 41.25 ± 2.80 dB, respectively (****$P < 0.0001$). Similar patterns were observed at 20 kHz (Control: 18.13 ± 2.49 dB vs. Non-tinnitus: 46.88 ± 2.82 dB vs. Tinnitus: 45.63 ± 4.06 dB; $F(4, 35) = 17.72$, ****$P < 0.0001$), 24 kHz (Control: 21.25 ± 2.46 dB vs. Non-tinnitus: 51.28 ± 2.63 dB vs. Tinnitus: 47.50 ± 2.11 dB; $F(4, 35) = 32.57$, ****$P < 0.0001$), and 32 kHz (Control: 23.13 ± 2.66 dB vs. Non-tinnitus: 50.00 ± 2.11 dB vs. Tinnitus: 51.25 ± 3.37 dB; $F(4, 35) = 25.46$, ****$P < 0.0001$). Critically, PBM induced no significant threshold changes in Non-tinnitus or Tinnitus mice across 10–32 kHz frequencies ($P > 0.05$), demonstrating that its therapeutic effects are not mediated by hearing restoration. These findings suggest alternative mechanisms, such as modulation of central auditory excitability or neuroplasticity, underlie PBM's efficacy in tinnitus alleviation.

PPI startle ratios were analyzed to exclude temporal processing deficit (Schilling et al., 2017). No intergroup differences in PPI% were observed across frequencies ($P > 0.05$), confirming tinnitus-related behaviors are not attributable to auditory processing impairments and PBM does not compromise sensory-motor gating (Fig. 3H, Supplementary Figure 1 C,D).

3.3. PBM Reverses auditory cortical hyperexcitability via suppression of tinnitus-associated GluN1 activation while preserving neuronal integrity

As a critical excitatory receptor in the auditory system, the overactivation of NMDARs is closely associated with the pathogenesis of tinnitus (Deng et al., 2020). Prolonged noise exposure or ototoxic drug-induced auditory dysfunction often triggers excessive NMDAR activation, which serves as a key contributor to tinnitus development. GluN1, an essential subunit for NMDAR functionality, is required for maintaining structural integrity and physiological activity of NMDARs. Loss of GluN1 disrupts NMDAR assembly, leading to functional impairment (Zhang et al., 2025). To investigate the role of NMDARs in noise-induced tinnitus, we performed double immunofluorescence co-staining for c-Fos and GluN1 in a tinnitus animal model induced by 1-hour 116 dB noise exposure centered at 16 kHz (Fig. 4A). In the non-tinnitus group, the proportion of c-Fos and GluN1 co-expressing neurons (59.57 ± 0.84 %) showed no significant difference compared to the control group (61.08 ± 1.33 %, Fig. 4B). However, the tinnitus group exhibited a marked increase in c-Fos/GluN1 co-expression within the AC (****$P < 0.0001$).

Subsequent immunohistochemical (IHC) analyses at multiple time points post-PBM were conducted to determine whether PBM could reverse AC hyperexcitability and alleviate tinnitus (Fig. 4C). In tinnitus animals treated with PBM, the percentage of c-Fos/GluN1 co-expressing neurons at 12, 24, 48, 96, and 144 h post-intervention was 79.05 ± 0.63 %, 79.16 ± 0.71 %, 74.36 ± 0.53 %, 71.11 ± 1.06 %, and 69.18 ± 0.62 %, respectively, $F(4, 40) = 38.29$, ****$P < 0.0001$ (Fig. 4D). Notably, PBM significantly reversed AC hyperexcitability commencing at 48 h post-treatment (***$P < 0.001$), with therapeutic effects peaking at 96 h (****$P < 0.0001$). No statistically significant difference was observed between 96 and 144 h ($P > 0.05$), indicating sustained efficacy over an extended period (>144 h after a single 5-minute irradiation). These results suggest that PBM exerts cumulative biological effects rather than immediate responses, with prolonged therapeutic maintenance. Based on these findings, the 96-hour time point was selected as the optimal window for further mechanistic exploration of PBM. Nissl staining was performed to assess whether noise-induced tinnitus caused auditory cortex neuronal death due to hyperexcitability (Fig. 4E). Neuronal death was not observed (91.89 ± 2.64, 95.33 ± 2.57, 96.78 ± 2.17; $F(2, 26) = 1.032$, $P = 0.3716 > 0.05$) (Fig. 4F). Furthermore, across all PBM treatment plans (Plan A-D), neuronal counts in tinnitus mice showed no significant change versus pre-treatment baselines (100.1 ± 2.01, 105.8 ± 3.10, 99.11 ± 2.28, 99.11 ± 1.70; $F(4, 40) = 1.533$, $P = 0.211 > 0.05$) (Figs. 4G, 4H).

To evaluate whether PBM selectively modulates AC excitability, we analyzed c-Fos/GluN1 co-expression via immunofluorescence staining in control and non-tinnitus groups (Fig. 5A). In the control group, no significant difference was observed in the proportion of c-Fos/GluN1 co-expressing neurons before (61.08 ± 1.33 %) and after PBM treatment (61.36 ± 0.70 %, $P = 0.8565 > 0.05$; Fig. 5B). The same result was observed in the Non-tinnitus group ($P = 0.7377 > 0.05$; Fig. 5C). Nissl staining further confirmed that PBM did not alter baseline neuronal counts in the control group (pre-PBM: 91.89 ± 2.64 vs. post-PBM: 89.89 ± 1.21, $P = 0.5018 > 0.05$; Fig. 5D, E) or non-tinnitus group (pre-PBM: 137.7 ± 2.98 vs. post-PBM: 129.7 ± 1.67, $P = 0.7453 > 0.05$; Fig. 5F, G). These findings collectively demonstrate that PBM exerts highly targeted neuromodulatory effects on the AC, likely reversing hyperexcitable neurons rather than broadly altering baseline neural activity.

We further investigated the regulatory effects of different PBM protocols (Plan-A to D) on AC excitability in tinnitus mice using c-Fos/GluN1 co-expression analysis (Fig. 5H). All protocols significantly reduced c-Fos/GluN1 co-expressing neurons post-PBM: Plan-A (77.00 ± 0.73 %), Plan-B (69.18 ± 0.62 %), Plan-C (78.21 ± 0.86 %), and Plan-D (70.54 ± 1.18 %) ($F(4, 40) = 62.76$, ****$P < 0.0001$; Fig. 5I). To explore the relationship between AC hyperexcitability and tinnitus-like behaviors in mice, linear regression analysis revealed a negative correlation between GPIAS% and c-Fos/GluN1 co-expression ($R^2 = 0.5464$, $P = 0.0016$; Fig. 5J). The upper-left quadrant of the regression plot

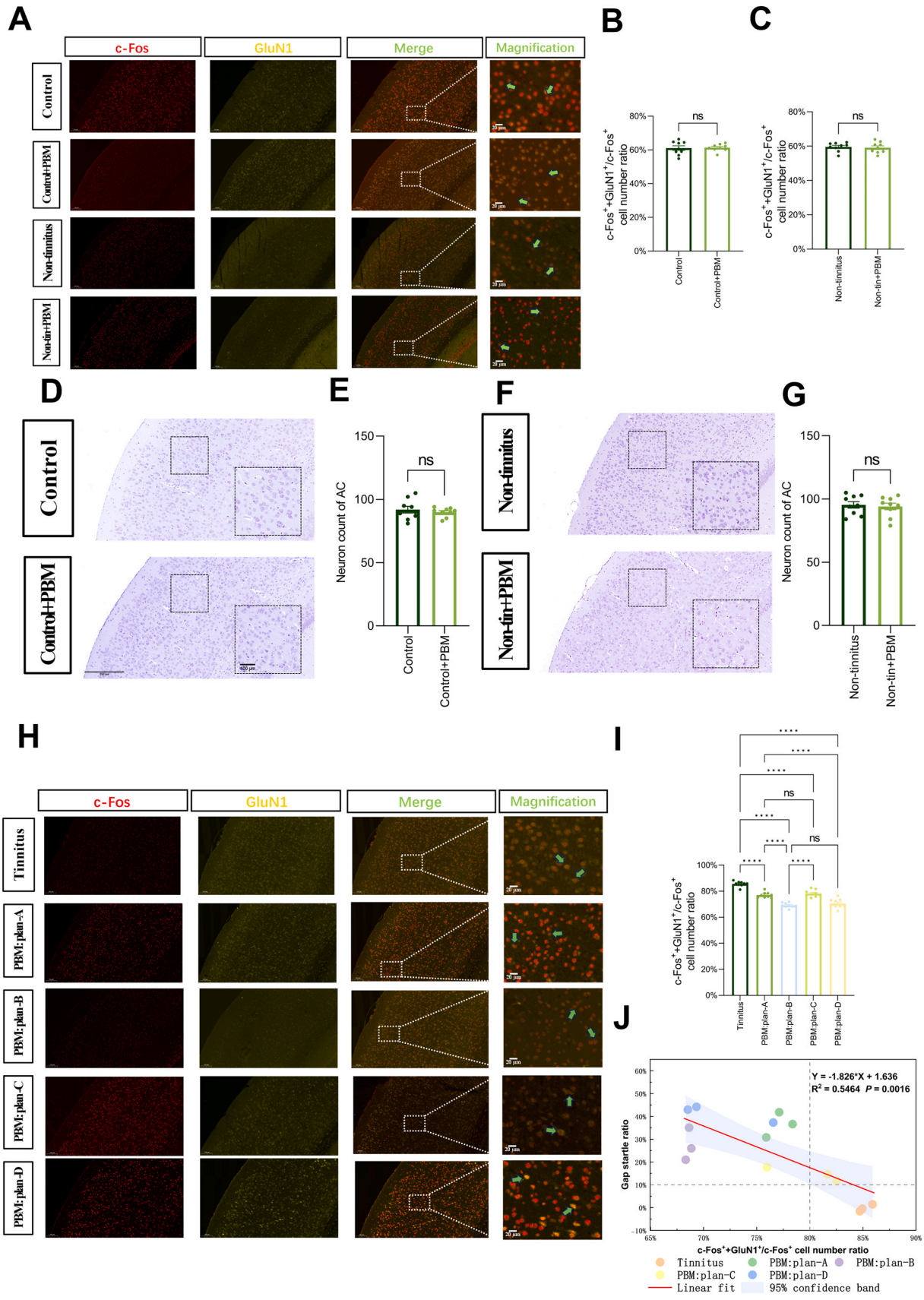

(caption on next page)

Fig. 5. A Representative coronal brain sections of AC showing c-Fos/GluN1 co-expression staining in sham noise-exposed control and noise-exposed non-tinnitus mice pre- and post-PBM. From left: sham control (Control), sham control with PBM (Control+PBM), noise-exposed non-tinnitus (Non-tinnitus), and noise-exposed non-tinnitus with PBM (Non-tin+PBM). PBM showed no significant effects on GluN1 receptor activation in either sham or non-tinnitus mice. Right panels: high-magnification views of AC. Scale bars: 250 μm (low) and 10 μm (high). B Quantitative analysis of c-Fos/GluN1 co-expression in AC of Control and Control+PBM groups (n = 6). C Quantitative analysis of c-Fos/GluN1 co-expression in AC of Non-tinnitus and Non-tin+PBM groups (n = 6). D Representative Nissl-stained AC sections from Control and Control+PBM groups. Scale bars: 250 μm (low) and 100 μm (high). E Quantification of Nissl-positive neurons in AC of Control and Control+PBM groups (n = 6). F Representative Nissl-stained AC sections from Non-tinnitus and Non-tin+PBM groups. Scale bars: 250 μm (low) and 100 μm (high). G Quantification of Nissl-positive neurons in AC of Non-tinnitus and Non-tin+PBM groups (n = 6). H Representative coronal sections of AC showing c-Fos/GluN1 co-expression in tinnitus mice pre- and post-PBM with four protocols (Plan A-D). Mid-to-high dose 830 nm PBM effectively reversed AC hyperexcitability. Right panels: high-magnification views. Scale bars: 250 μm (low) and 10 μm (high; n = 15). I Quantitative analysis of c-Fos/GluN1 co-expression in AC of Tinnitus, PBM:Plan-A, PBM:Plan-B, PBM:Plan-C, and PBM:Plan-D groups (n = 15). J Linear correlations between c-Fos/GluN1 co-expression in AC and GPIAS% across PBM protocols (n = 15). Statistical annotations: ns ($P > 0.05$); *$P < 0.05$; **$P < 0.01$; ***$P < 0.001$; ****$P < 0.0001$. Error bars represent SEM.

represents low tinnitus-like behavior probability with reversed AC hyperexcitability, while the lower-right quadrant reflects the opposite pattern. These results highlight Plan-B's superior therapeutic efficacy in tinnitus treatment. Our findings indicate that tinnitus-like behaviors are associated with GluN1-mediated mechanisms, and PBM effectively reverses AC hyperexcitability in tinnitus mice.

3.4. Quantitative phosphoproteomics identifies synaptic restructuring and transmembrane ion transport as PBM-mediated therapeutic targets via neuronal membrane receptors

To investigate molecular differences among control, tinnitus, and PBM-treated mice, we performed phosphoproteomic analysis on AC tissues (Fig. 6A). Each group included six mice, with pooled right AC samples from two mice per replicate to ensure sufficient protein quantities. No significant differences in relative standard deviation (RSD) were observed between groups (Fig. 6B). A total of 10,984 modified peptides corresponding to 3054 quantifiable proteins were identified (Fig. 6C). Intergroup comparisons revealed distinct global phosphorylation patterns, suggesting that PBM alleviates tinnitus by modulating protein phosphorylation (Fig. 6D). K-means clustering of differentially phosphorylated proteins segregated them into four clusters (Fig. 6E). Notably, cluster 3 exhibited tinnitus-specific phosphorylation changes absent in control and PBM groups, implicating these proteins as potential key mediators of PBM efficacy. KEGG pathway analysis of cluster 3 highlighted strong associations with GABAergic, glutamatergic, and cholinergic synaptic pathways (Fig. 6F). These findings propose a multitarget mechanism for PBM: rebalancing AC excitatory/inhibitory (E/I) equilibrium through a tripartite network involving enhanced inhibitory transmission (GABAergic), restored excitatory homeostasis (glutamatergic), and optimized higher-order modulation (cholinergic), thereby driving adaptive synaptic remodeling.

Statistical analysis of phosphorylation differences across groups identified 29 shared phosphorylation sites among control, tinnitus, and PBM mice (Fig. 7B). Compared to controls, tinnitus mice showed increased phosphorylation at 141 sites and decreased phosphorylation at 1066 sites (Fig. 7A), including upregulated Grin2b-S1116 (NMDA receptor subunit 2B), Rac1-T108 (Ras-related C3 botulinum toxin substrate 1), and Map2-S496 (microtubule-associated protein 2), alongside downregulated Dlg4-S654 (postsynaptic density protein 95), Dlg2-S406 (postsynaptic density protein 93), and Dlgap1-S421 (postsynaptic density-associated protein 1). These alterations indicate profound synaptic structural reorganization in tinnitus mice. Following PBM treatment, tinnitus mice exhibited increased phosphorylation at 125 sites and decreased phosphorylation at 81 sites (Fig. 7C), marked by upregulated Camk2b-T287 (calcium/calmodulin-dependent protein kinase IIβ), Gap43-T172 (growth-associated protein 43), Shank1-S788, Shank3-S11539, and downregulated Grin2a-S1062 (NMDA receptor subunit 2 A). Gene Ontology (GO) enrichment analysis further differentiated biological processes, cellular components, and KEGG pathways between control vs. tinnitus and tinnitus vs. PBM groups, emphasizing synaptic architecture and transmembrane ion transport (Fig. 7D-I).

3.5. PBM mitigates neuronal structural complexity by restoring synaptic plasticity equilibrium

Building on our phosphoproteomic findings implicating synaptic plasticity in tinnitus pathogenesis and PBM-mediated therapeutic modulation, we further validated these observations morphologically. Noise-induced tinnitus significantly disrupted synaptic plasticity homeostasis in the AC, characterized by aberrant synaptic proliferation, ultrastructural remodeling of PSD regions (increased thickness and area), and elongated active zones (Fig. 8A-G). These pathological features align with prior reports of noise-induced glutamatergic hyperactivation and neural network reorganization (Yi et al., 2018). TEM revealed that tinnitus mice exhibited a 3.3-fold increase in synaptic density ($F(2, 27) = 104$, ****$P < 0.0001$), alongside significantly elevated PSD thickness (48.19 ± 2.89 nm) and area ($28{,}732 \pm 1297$ nm^2) (****$P < 0.0001$), indicative of synaptic overpotentiation and hyperexcitable signaling. Strikingly, PBM treatment reversed these alterations: PSD thickness and area in PBM-treated mice recovered to 135 % and 115 % of control levels, respectively (****$P < 0.0001$, PBM vs. tinnitus), with synaptic density markedly reduced (6.00 ± 0.42 vs. 15.40 ± 0.76 in tinnitus, ****$P < 0.0001$), demonstrating PBM's capacity to rebalance synaptic plasticity via GluN1 activity modulation.

Golgi staining further demonstrated that PBM selectively corrected tinnitus-associated axonal branching anomalies (reduced branch number and total length, ****$P < 0.0001$, PBM vs. tinnitus) without affecting dendritic spine density ($P = 0.9803$; Fig. 8H-M). This specificity suggests that PBM restores neural network integrity by preferentially regulating presynaptic architecture and PSD remodeling rather than globally suppressing synaptic plasticity. These structural insights support a targeted therapeutic mechanism whereby PBM inhibits maladaptive synaptic ultrastructural overcompensation, thereby reinstating excitatory-inhibitory (E/I) equilibrium. Collectively, our findings establish PBM as a non-invasive neuromodulatory strategy that mitigates tinnitus-related central auditory hyperexcitability by rectifying synaptic plasticity imbalances, including PSD hypertrophy, synaptic hyperproliferation, and aberrant axonal arborization.

3.6. GluN1 contributes to tinnitus pathogenesis while maintaining physiological auditory information processing

To validate the pivotal role of GluN1 in tinnitus development, we utilized recombinant adeno-associated viral (rAAV) vectors encoding GluN1-overexpressing short hairpin RNA (rAAV-Grin1) (Fig. 9A-G). Gap startle tests in naïve mice revealed tinnitus-like behaviors in 6 of 7 rAAV-Grin1-injected animals (85.71 % incidence, detectable across 10 frequencies), with pronounced GPIAS% reductions at 10, 12, and 20 kHz and similar trends at other frequencies (Fig. 9H). No tinnitus-like behaviors were observed in control virus-injected mice (Fig. 9I). PPI startle tests confirmed that GluN1 overexpression did not impair auditory information processing, mirroring observations from noise-induced tinnitus models (Supplementary Figure 1E,F).

We further mimicked PBM-mediated GluN1 suppression using rAAV vectors encoding GluN1-targeting shRNA (rAAV-shRNA(Grin1)) to

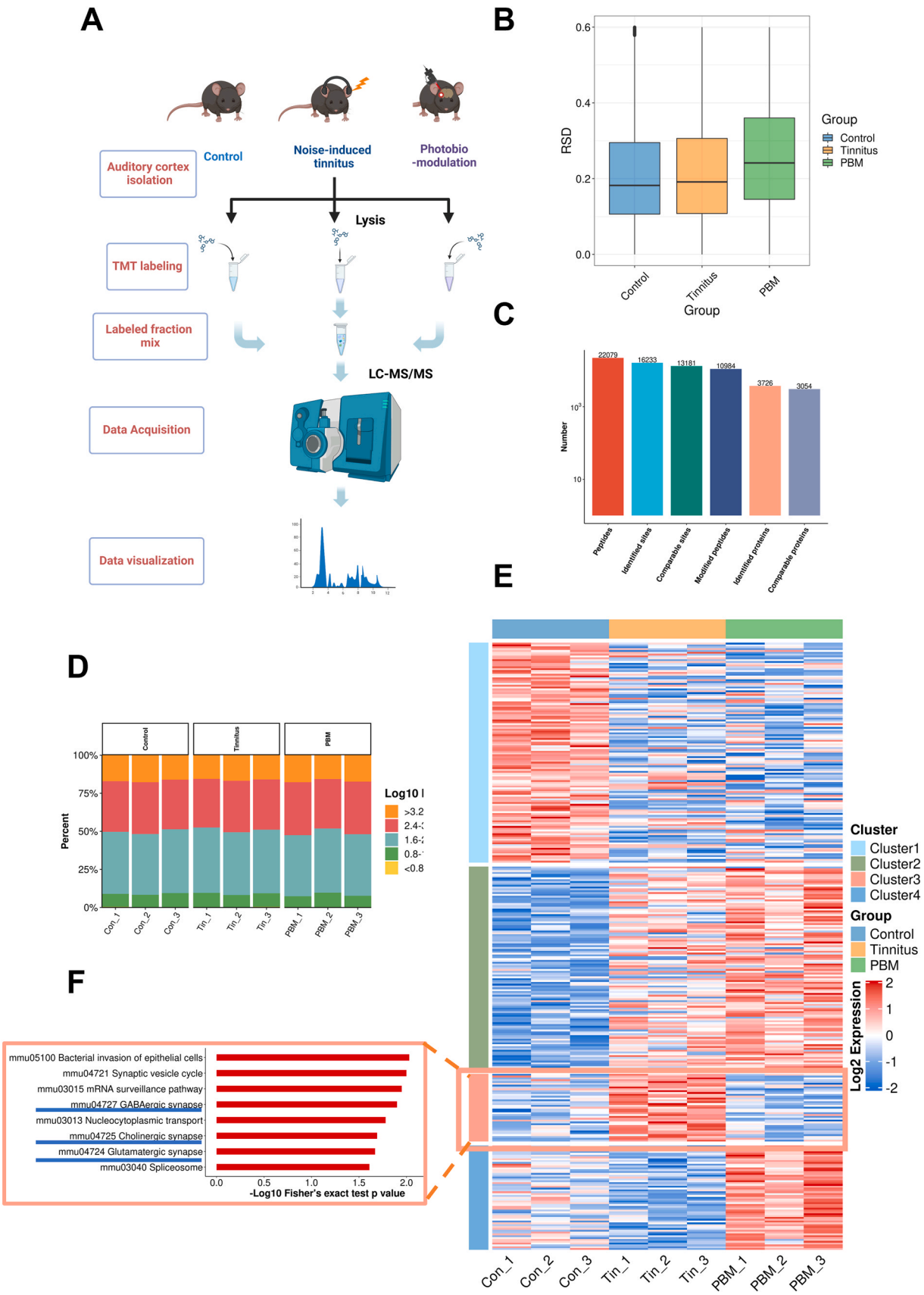

Fig. 6. A Schematic workflow of phosphoproteomic analysis (n = 18). B RSD across control, tinnitus, and PBM groups. C Number of identified phosphopeptides and phosphorylation sites. D Stacked bar plot showing distribution and abundance of modified sites. E, F Heatmap of k-means clustering results (E). Differentially phosphorylated proteins were grouped into four clusters. Proteins with tinnitus-specific phosphorylation changes (pink boxes) and their most significantly enriched KEGG pathways are displayed as bar plots (F). Pathways most relevant to this study are highlighted with blue horizontal lines.

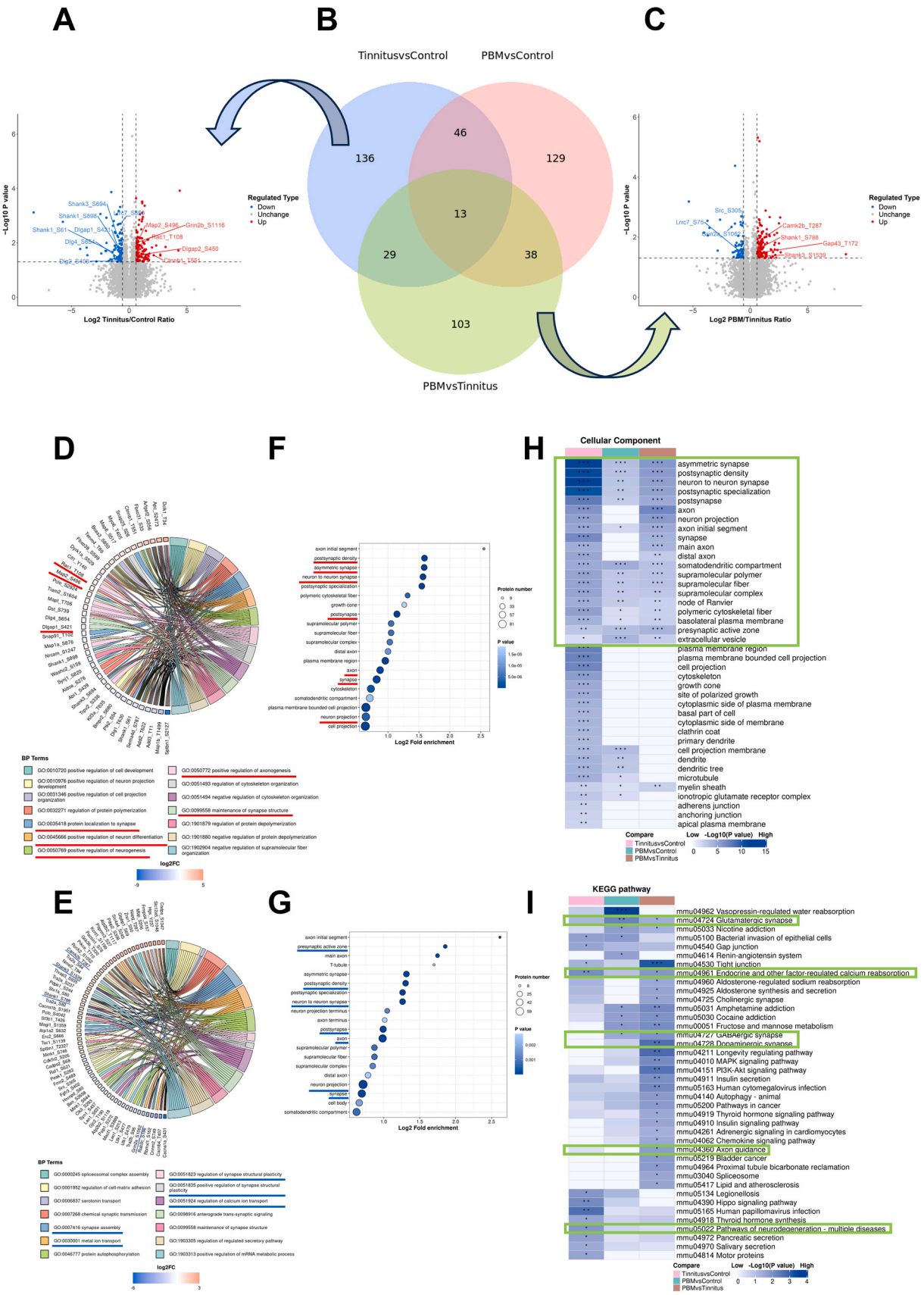

(caption on next page)

Fig. 7. A Volcano plot comparing phosphopeptide reporter ion intensity ratios (Tinnitus vs. Control) against p-values. Colored dots represent significantly altered phosphopeptides (red: upregulated; blue: downregulated). B Venn diagram of differentially expressed phosphopeptides among control, tinnitus, and PBM groups. C Volcano plot comparing phosphopeptide reporter ion intensity ratios (PBM vs. Tinnitus) against p-values. Colored dots follow the same scheme as panel A. D, E Chord diagrams illustrating relationships between significantly enriched Biological Processes (BP) and phosphorylation sites for Tinnitus vs. Control (D) and PBM vs. Tinnitus (E). BPs are listed on the right, with connected phosphorylation sites ordered by descending log2 fold change (Log2FC). Key BPs are marked with red/blue horizontal lines. F, G Bubble plots of enriched Cellular Component (CC) terms for Tinnitus vs. Control (F) and PBM vs. Tinnitus (G). Y-axis: CC descriptions; X-axis: log2-transformed fold enrichment. Bubble color indicates p-value significance (darker blue = higher significance); size reflects the number of differentially modified proteins. Critical CC terms are highlighted with red/blue lines. H, I Heatmaps displaying functional enrichment clusters for phosphorylated proteins based on CC (H) and KEGG pathways (I). Color intensity reflects enrichment significance (blue = high; pale blue = low). Asterisks denote statistical thresholds: $*P < 0.05$; $**P < 0.01$; $***P < 0.001$. Key terms are outlined with green boxes.

assess its therapeutic relevance (Supplementary Figure 2A-F). Gap startle tests in tinnitus mice showed partial behavioral remission (4/14 frequencies improved, 28.57 %), though most frequencies exhibited persistent deficits (8/14 frequencies worsened, 57.14 %; Supplementary Figure 2 G). Control virus-injected tinnitus mice displayed no behavioral changes (Supplementary Figure 2H). Notably, PPI% significantly declined following GluN1 knockdown ($**P < 0.01$; Supplementary Figure 2I, J), demonstrating GluN1's necessity for maintaining physiological auditory processing. These findings establish GluN1 as both a driver of tinnitus pathogenesis and an essential regulator of normal auditory function, highlighting the precision required for therapeutic targeting.

4. Discussion

In this study, we employed a noise-induced tinnitus model to examine the effects of PBM on auditory cortex function. Our findings indicate that transcranial PBM at 40 mW/cm^2 reduced noise-induced neuronal hyperactivity in the auditory cortex while maintaining normal hearing thresholds. This effect appears to involve modulation of GluN1-containing NMDA receptors and restoration of synaptic function. Phosphoproteomic analysis further revealed changes in proteins related to synaptic structure and ion transport. Aberrant neuronal hyperexcitability plays a pivotal role in tinnitus pathogenesis (Yu et al., 2024). Using double immunofluorescence co-staining, we monitored noise-induced AC hyperexcitability, which arises from maladaptive neural encoding mechanisms in this higher-order auditory integration hub. Peripheral auditory insults trigger synaptic reorganization and enhanced neural network synchronization in the AC, manifesting as cross-frequency neuronal ensemble coupling anomalies and tonotopic map distortions (Xie et al., 2025). Such pathological network remodeling may drive misinterpretation of spontaneous neural signals by central auditory circuits, ultimately generating subjective tinnitus perception.

Our findings align with prior evidence that noise exposure induces glutamatergic synaptic potentiation, GABAergic disinhibition, and dysregulated NMDAR phosphorylation, collectively establishing a "disinhibition-hyperexcitation" circuit state (Rafe et al., 2024; Cao et al., 2024; Zhang et al., 2021). This excitatory imbalance amplifies central gain for spontaneous electrical activity, enabling cortical neuronal populations to aberrantly encode subthreshold signals, thereby perpetuating tinnitus perception. Notably, our phosphoproteomic profiling revealed that PBM restores synaptic E/I balance by modulating phosphorylation cascades in GABAergic, glutamatergic, and cholinergic pathways—a tripartite mechanism that rectifies pathological network hyperactivity without compromising baseline auditory processing.

The AC's role as a neural integrator underscores its susceptibility to noise-induced plasticity. Our ultrastructural analyses demonstrated that PBM selectively reverses synaptic overpotentiation (e.g., PSD hypertrophy) and axonal arborization anomalies, suggesting spatiotemporal precision in its therapeutic action. Crucially, GluN1 knockdown experiments highlighted the receptor's dual role: while its overactivation drives tinnitus, physiological GluN1 activity remains indispensable for normal auditory information processing. This dichotomy emphasizes the need for targeted neuromodulation strategies like PBM, which attenuate maladaptive plasticity while preserving essential neural functions.

Excessive neuronal activity promotes the overrelease of neurotransmitters from presynaptic membranes, leading to overactivation of postsynaptic receptors and subsequent phosphorylation and remodeling of postsynaptic proteins such as PSD-95. This cascade drives the formation of new synaptic connections, manifesting as increased synaptic structural complexit (De Carvalho et al., 2024). Such aberrant connectivity may disrupt normal neural circuitry, contributing to information-processing dysfunction and perpetuating tinnitus. To explore this, we employed TEM and Golgi staining to assess synaptic ultrastructure and dendritic/axonal morphology in tinnitus mice pre- and post-PBM treatment. Noise-induced tinnitus mice exhibited abnormal synaptic proliferation, enlarged PSD dimensions (thickness and area), and elongated active zones. In contrast, AC neurons treated with 830 nm laser-based PBM displayed reduced PSD hypertrophy and diminished aberrant axonal connectivity. These findings underscore PBM's potential neuroprotective utility in mitigating noise-induced AC hyperexcitability and associated neuronal pathologies.

Our study focuses on non-invasive neuromodulation, particularly neuronal excitability regulation, using noise-induced tinnitus as a model. Neuromodulatory techniques, by targeting maladaptive plasticity in tinnitus-related neural circuits, offer innovative therapeutic strategies. Prior studies demonstrate that non-invasive approaches such as TMS and transcranial direct current stimulation (tDCS) selectively modulate AC excitability through mechanisms involving NMDAR-dependent long-term depression (LTD) reinstatement (Han et al., 2025; Kweon et al., 2023; Latchoumane et al., 2018). Compared to conventional pharmacotherapy, neuromodulation provides advantages including superior spatiotemporal resolution, reversibility, and controllable side effects (Yang et al., 2025). While further optimization of stimulation parameters and personalized protocols is warranted, this technology represents a promising avenue for unraveling tinnitus chronicity mechanisms and advancing precision medicine interventions.

PBM offers a novel non-invasive neuromodulatory strategy by targeting mitochondrial function and membrane receptor proteins in neurons. Its mechanism involves red and near-infrared light modulation of CCO, promoting nitric oxide (NO) synthesis, reducing cellular inflammation, and regulating neuronal excitability via membrane receptor-mediated ion signaling pathways (Feng et al., 2024; Hamblin, 2024). To explore these effects, we developed a non-invasive, low--intensity optogenetic device with ultrahigh spatial resolution (~0.5 mm) and minimal operational power (~5 mW), demonstrating potential for cross-disease modeling and clinical translation. Using this platform, we investigated PBM's regulatory effects on AC excitability. Our findings revealed that PBM's biological efficacy depends critically on specific IP thresholds rather than RE. Moreover, prolonged ED does not linearly enhance therapeutic outcomes, likely due to PBM's biphasic dose-response relationship—a phenomenon consistent with the Arndt-Schulz law (Stebbing, 1982). Subthreshold light doses yield negligible effects, moderate doses induce beneficial responses until saturation, and suprathreshold doses progressively diminish benefits, eventually causing tissue damage. This biphasic response underscores the necessity for precise IP-ED-RE parameterization in clinical PBM applications to avoid adverse effects.

Notably, at our optimized IP of 40 mW/cm^2, PBM predominantly exerted inhibitory neuromodulation, aligning with Hamblin et al.'s

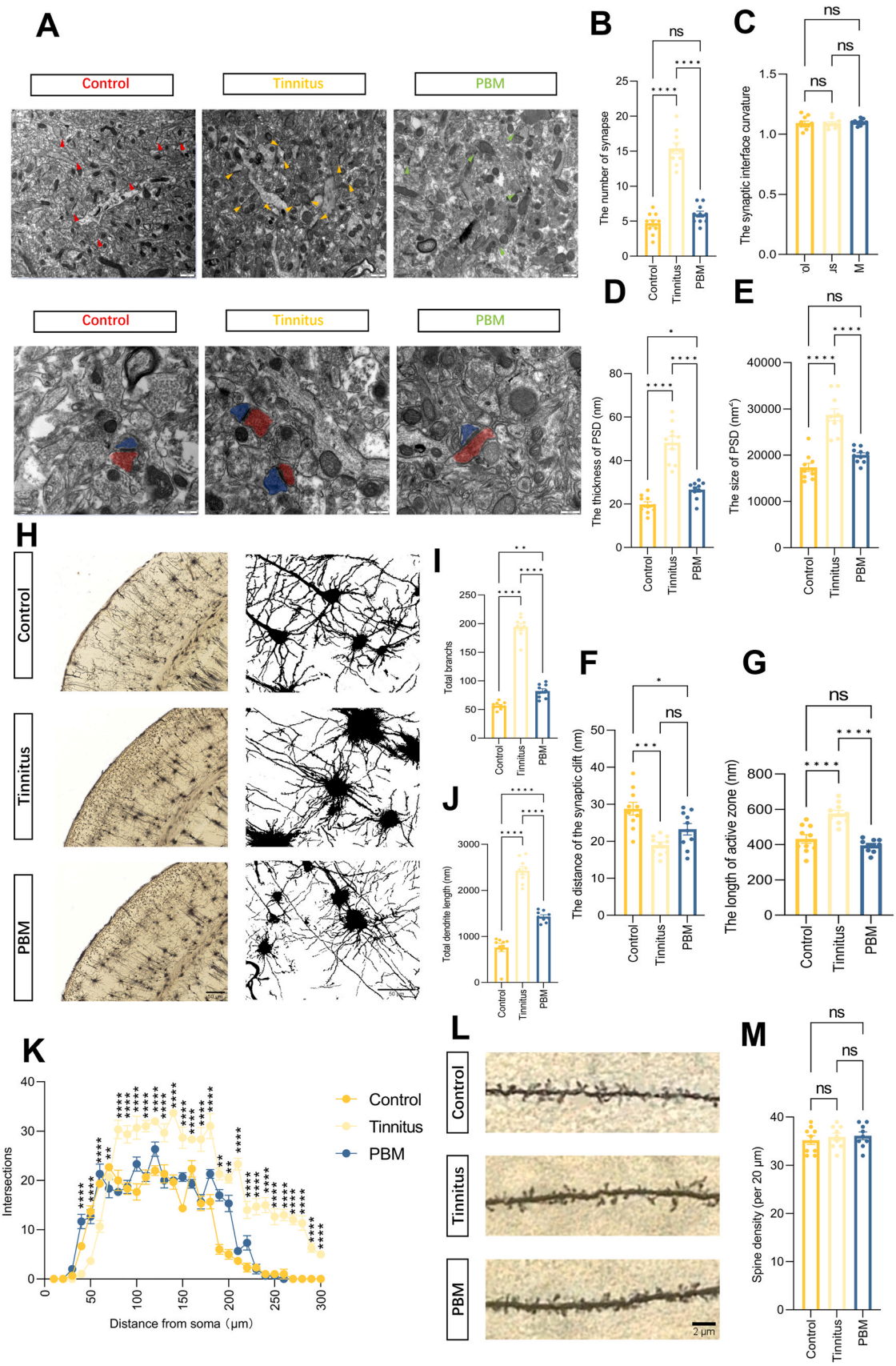

(caption on next page)

Fig. 8. A Representative TEM images of AC in Control, Tinnitus, and PBM groups. Top row: low-magnification views (×16,000; scale bar = 1 μm). Bottom row: high-magnification views (×30,000; scale bar = 500 nm). Arrows indicate synapses. Pseudocolored regions: red (presynaptic structures), blue (postsynaptic structures). B Quantification of synaptic density under low magnification across groups (n = 9). C-G Ultrastructural parameter analyses of AC synapses, including synaptic curvature, PSD thickness, PSD area, synaptic cleft distance, and active zone length in Control, Tinnitus, and PBM groups. H Golgi-stained hippocampal micrographs from Control, Tinnitus, and PBM groups. Dendritic branches were skeletonized, and complexity was quantified using ImageJ. Scale bar = 50 μm (n = 9). I-K Representative skeletonized hippocampal neurons and Sholl analysis of dendritic complexity. Metrics include branch number, total branch length, and branching patterns within 0–300 μm from the soma center. L, M Representative dendritic spine images and spine density measurements across groups. Scale bar = 2 μm (n = 9). Statistical annotations: ns ($P > 0.05$); *$P < 0.05$; **$P < 0.01$; ***$P < 0.001$; ****$P < 0.0001$. Error bars represent SEM.

findings where 25 mW/cm^2 PBM protected primary cortical neurons from glutamate-induced excitotoxicity (Huang et al., 2014). Conversely, Mohammed H. S. et al. reported that 127.4 mW/cm^2 PBM attenuated monoamine depletion and oxidative stress in a reserpine-induced depression model after two-week daily irradiation (Mohammed and Khadrawy, 2022). While existing studies hint at single-parameter threshold effects, the dynamic interplay among IP, RE, and ED remains poorly understood. Future research should systematically map the IP-RE-ED three-dimensional parameter space, integrating real-time metabolic imaging and molecular dynamics simulations to quantitatively resolve the structure-activity relationships governing photon energy transfer and neuroplasticity modulation. Such efforts will establish a precision framework for PBM's clinical translation.

Noise-induced hearing loss, a major contributor to tinnitus pathogenesis, involves not only mechanical damage to the peripheral auditory system but also aberrant activation of central gain mechanisms via enhanced glutamatergic synaptic transmission in the AC. This neuroplastic remodeling establishes a persistent cortical hyperexcitability state, which is strongly associated with tinnitus chronicity. Furthermore, functional decoupling of prefrontal-temporal neural networks may mediate attentional deficits and reduced working memory capacity, forming the pathological basis for tinnitus-cognitive comorbidity (Rosická et al., 2024; Du et al., 2024). Morphometric analyses in our noise-induced tinnitus model revealed increased numbers of GluN1-activated neurons in the AC compared to sham controls. PBM treatment reduced the number of GluN1-activated neurons starting at 48 h post-intervention, with maximal therapeutic effects peaking beyond 96 h and lasting at least 144 h. Critically, our study demonstrates that PBM effectively suppresses pathological synaptic ultrastructural overcomplexity in tinnitus mice, such as aberrant axonal connectivity. These findings complement prior work by Zhang et al., who showed that 810 nm PBM (5.76 J/cm^2) restored synaptic interface curvature in a hippocampal aging model (Zhang et al., 2022a). Together, these studies highlight the parameter-dependent modulation of synaptic ultrastructure by PBM, suggesting its potential for bidirectional regulation through optimized irradiation parameters. For instance, while our protocol (40 mW/cm^2) attenuated maladaptive axonal sprouting in tinnitus, Zhang's parameters enhanced synaptic repair in neurodegeneration. This duality underscores the need for rigorous parameterization to align PBM's effects with specific pathological contexts. The sustained suppression of GluN1 activation observed here—lasting over 144 h after a single PBM session—implies durable neuromodulatory effects distinct from conventional pharmacological interventions. Such prolonged efficacy may stem from PBM's ability to reset maladaptive synaptic plasticity thresholds, thereby interrupting the positive feedback loop between central hyperexcitability and tinnitus perception. Future studies should explore whether repeated PBM sessions synergize with cognitive-behavioral therapies to address both tinnitus and its comorbid cognitive deficits.

Our phosphoproteomic profiling revealed minimal differences in protein phosphorylation between control and PBM-treated groups (Fig. 6D), suggesting that PBM selectively modulates synaptic plasticity without perturbing baseline physiology. In contrast, distinct phosphorylation patterns emerged in noise-induced tinnitus mice, which were significantly altered post-PBM. These results unequivocally demonstrate PBM's unique therapeutic action under pathological conditions. Immunofluorescence staining confirmed markedly elevated GluN1 protein levels in tinnitus mice, consistent with hyperexcitability. Beyond GluN1, phosphorylation changes in GluN2 subtypes critically contributed to tinnitus pathogenesis and treatment. Specifically, elevated GluN2B (NMDA receptor subunit 2B) phosphorylation in tinnitus mice enhanced NMDA receptor-mediated calcium influx, driving neuronal hyperexcitability.

Downstream of GluN2B, upregulated Rac1 phosphorylation likely promoted aberrant axonal branching and presynaptic structural disorganization by dysregulating actin dynamics in axonal growth cones (Zhang et al., 2022b). Concurrently, heightened Map-2 phosphorylation disrupted microtubule polarity in axonal transport, leading to abnormal presynaptic vesicle distribution (Meng et al., 2023). Conversely, reduced phosphorylation of PSD95 and Dlgap1 destabilized molecular anchoring between postsynaptic densities and presynaptic active zones. PSD95, which couples postsynaptic NMDARs to presynaptic neurexin/neuroligin complexes, exhibited impaired functionality that may compromise trans-synaptic signaling precision (Nam and Chen, 2005). Similarly, aberrant Dlgap1 modifications exacerbated mechanical decoupling of pre- and postsynaptic structures (Coba et al., 2018). This cascade illustrates that GluN2B overactivation not only directly potentiates presynaptic neurotransmitter release but also fosters a vicious cycle of electrical activity-axonal remodeling via Rac1/Map-2-mediated structural distortions and PSD95/Dlgap1-dependent synaptic destabilization. Such maladaptive plasticity may irreversibly entrench pathological neural circuits, perpetuating tinnitus. Our findings align with emerging evidence that PBM's parameter-dependent modulation of synaptic ultrastructure—evidenced here and in prior studies—offers a tunable strategy to disrupt this cycle.

This study utilized the GPIAS paradigm to assess tinnitus-like behavior. While this method provides valuable behavioral evidence of tinnitus, it has limitations as it cannot fully distinguish tinnitus from other auditory processing deficits. To further strengthen the translational potential of our findings, future studies should validate these results using complementary behavioral models such as conditioned suppression paradigms, combined with direct physiological measures of neural activity (Longenecker et al., 2018).

Clinically, effective pharmacological and therapeutic interventions for tinnitus remain scarce, with current strategies predominantly limited to neurotrophic agents and microcirculation improvement (Sherlock et al., 2025). However, most tinnitus patients exhibit poor responsiveness to these treatments. Given its non-invasive nature, PBM could offer broad therapeutic benefits for tinnitus patients and those with comorbid neuroexcitability disorders if its neuromodulatory efficacy on the AC is validated. This study highlights several critical limitations. First, standardized protocols for PBM parameters—particularly the synergistic effects of IP and ED—remain undefined, necessitating systematic exploration of differential biological outcomes across parameter combinations. Second, while current efficacy assessments focus on acute effects of single-session interventions, the cumulative benefits and potential tolerance thresholds of repeated treatments require validation through stepwise dosing protocols. Finally, the precise therapeutic window of single PBM sessions lacks delineation, underscoring the need to establish time-dependent dynamic models of neuroplasticity. Addressing these gaps will refine PBM's translational potential, enabling personalized parameter optimization for heterogeneous patient populations.

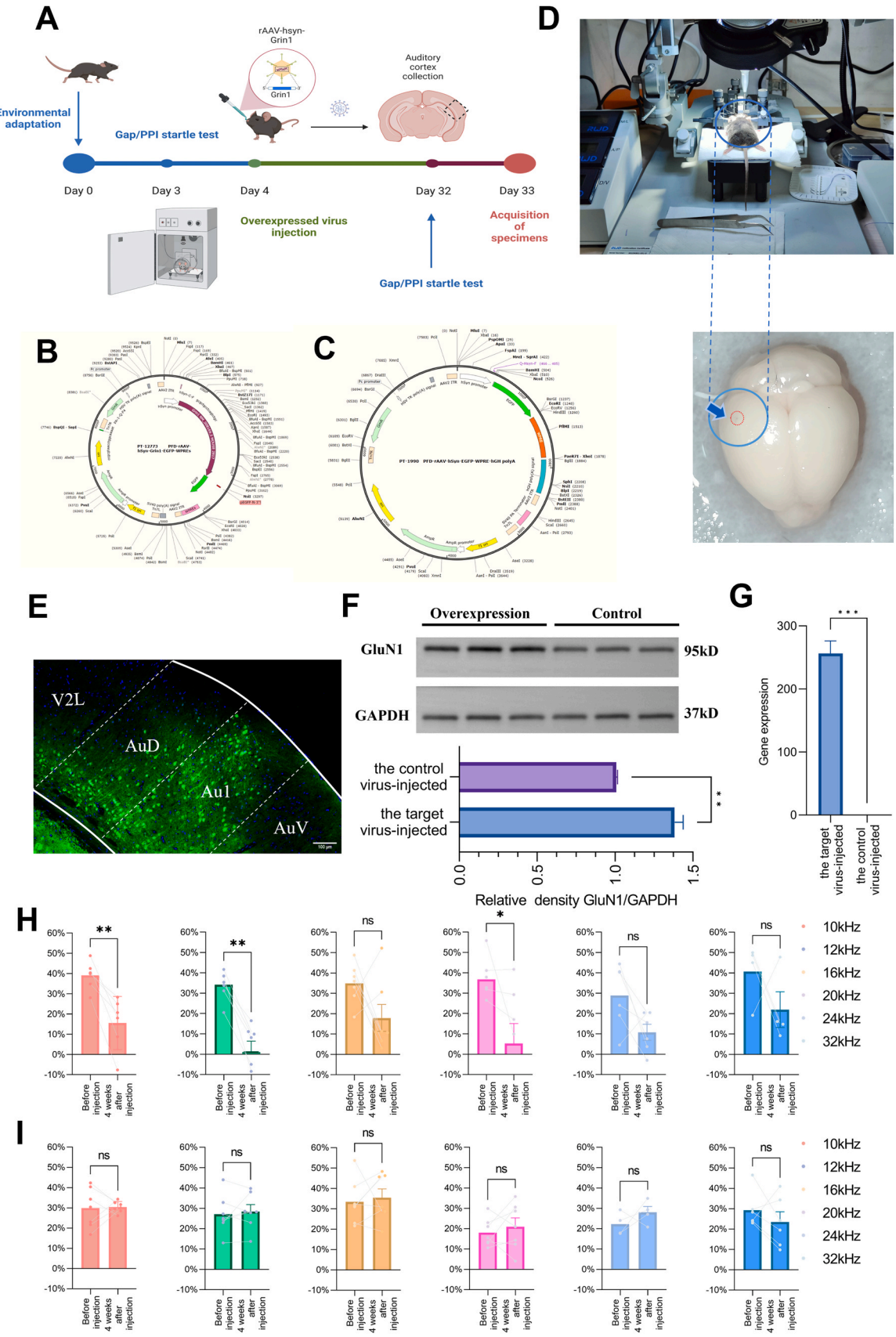

Fig. 9. A Experimental timeline schematic. B, C Genetic architectures of target (rAAV-hsyn-Grin1-EGFP-WPREs) and control (PFD-rAAV-hSyn-EGFP-WPRE-hGH polyA) viral vectors. D In vivo visualization of viral injection. E Exogenous GluN1 expression in AC via rAAV-hsyn-Grin1-EGFP-WPREs/PFD-rAAV-hSyn-EGFP-WPRE-hGH polyA. Scale bar = 100 μm (n = 2). F Validation of GluN1 protein levels by western blot (n = 6). G Verification of GluN1 transcript levels by qPCR (n = 6). H, I GPIAS% startle ratios in target virus-injected (H, n = 7) and control virus-injected (I, n = 7) mice pre- vs. post-injection.

5. Conclusions

This study demonstrates that low-intensity PBM penetrates the skull to modulate the central nervous system, with stable post-cranial optical properties across varying IP levels, establishing a physical foundation for non-invasive neuromodulation. At an optimized IP of 40 mW/cm^2, PBM effectively alleviated noise-induced AC hyperexcitability in a tinnitus model while preserving hearing thresholds and auditory information processing, underscoring its biosafety. Mechanistically, PBM restored synaptic plasticity equilibrium by selectively inhibiting pathological hyperactivation of the GluN1 subunit of NMDA receptors, thereby reversing excessive glutamatergic synaptic transmission. Quantitative phosphoproteomic profiling further revealed that PBM reduces neuronal structural complexity by regulating synaptic ultrastructure (e.g., PSD thickness, axonal branching patterns) and modifying transmembrane ion transport-related proteins, ultimately restoring neural network functional integration. Notably, GluN1 exhibits dual roles in tinnitus pathogenesis: its overactivation drives pathological hyperexcitability, while its physiological expression is essential for maintaining normal auditory processing. PBM achieves a therapeutic balance by precisely modulating GluN1 activity, enabling selective suppression of maladaptive plasticity without compromising baseline neural function. These findings highlight PBM's bidirectional regulatory mode—inhibiting aberrant synaptic remodeling while preserving fundamental neural activity—as a novel strategy for tinnitus treatment that combines precision and clinical feasibility. Given its non-invasiveness, tunable parameters, and sustained efficacy (>144 h post-intervention), PBM emerges as a promising candidate for clinical translation in subjective tinnitus. Future studies should focus on parameter optimization and validation of long-term therapeutic durability to accelerate its application in addressing unmet clinical needs.

CRediT authorship contribution statement

Li Wang: Writing – original draft, Visualization, Validation. **Hanwen Zhou:** Investigation, Formal analysis, Data curation, Conceptualization. **Weidong Shen:** Software, Resources. **Peng Liu:** Validation, Supervision, Project administration, Methodology, Investigation. **Chi Zhang:** Writing – original draft, Software, Project administration, Methodology. **Yvke Jiang:** Writing – review & editing, Writing – original draft, Software, Data curation, Conceptualization. **Shuhan Lv:** Writing – original draft, Visualization. **Shiming Yang:** Writing – review & editing, Writing – original draft, Software, Resources, Project administration. **Fangyuan Wang:** Writing – review & editing, Writing – original draft, Funding acquisition, Conceptualization. **Zhixin Zhang:** Writing – review & editing, Writing – original draft, Visualization, Resources, Project administration, Conceptualization. **Xinmiao Xue:** Writing – review & editing, Writing – original draft, Resources, Methodology, Investigation. **Dongdong He:** Writing – review & editing, Writing – original draft, Formal analysis, Data curation, Conceptualization.

Ethics approval and consent to participate

Not applicable.

Consent for publication

Not applicable.

Funding

This research was financially supported by the National clinical Research center for Otolaryngologic Diseases, State Key Laboratory of Hearing and Balance Science, Astronaut Health Center Key Laboratory Research Fund (Project: AHCC2021KF002), the National Key Research and Development Program (Project: 2022YFC2402704, and 2022YFC2402701).

Declaration of Competing Interest

The authors declare that they have no known competing financial interests or personal relationships that could have appeared to influence the work reported in this paper.

Acknowledgments

All authors were involved in the design of this research. All authors read and approved the final manuscript. We extend our heartfelt gratitude to Prof. Shiming Yang and Prof. Fangyuan Wang for their insightful comments and dedication in preparing the manuscript. Additionally, we acknowledge the support of Jintao Li, Minyue Qiu , Xiaotang Fan and Chuanqi Liu from the Army Medical University, whose assistance was instrumental in initiating this research.

Appendix A. Supporting information

Supplementary data associated with this article can be found in the online version at doi:10.1016/j.brainresbull.2025.111685.

Data availability

This manuscript reports data based on original published studies and the viewpoints of individual researchers who contributed to the workshop. The corresponding author, Fangyuan Wang, may be contacted for further information.

References

Arifin, W.N., Zahiruddin, W.M., 2017. Sample size calculation in animal studies using resource equation approach. Malays. J. Med Sci. 24 (5), 101–105.
Barrett, D.W., Davis, R.E., Siegel-Ramsay, J.E., et al., 2025. Cognitive improvement and prefrontal network interactions in individuals with remitted bipolar disorder after transcranial infrared laser stimulation. Front. Psychiatry 16, 1547230.
Batts, S., Stankovic, K.M., 2024. Tinnitus prevalence, associated characteristics, and related healthcare use in the United States: a population-level analysis. Lancet Reg. Health Am. 29, 100659.
Cao, W., Xiong, S., Ji, W., et al., 2024. Neuroprotection role of Vitamin C by upregulating Glutamate Transporter-1 in auditory cortex of noise-induced tinnitus animal model. ACS Chem. Neurosci. 15 (6), 1197–1205.
Chen, C.H., Hadi, H., 2021. An evaluation method for meeting the requirement of IEC 60825-1 laser safety standard for viewing temporally-varied radiant power. Health Phys. 121 (1), 1–6.
Coba, M.P., Ramaker, M.J., Ho, E.V., et al., 2018. Dlgap1 knockout mice exhibit alterations of the postsynaptic density and selective reductions in sociability. Sci. Rep. 8 (1), 2281.
Creed, R.B., Roberts, R.C., Farmer, C.B., et al., 2021. Increased glutamate transmission onto dorsal striatum spiny projection neurons in Pink1 knockout rats. Neurobiol. Dis. 150, 105246.
De Carvalho, M.B., Teixeira-Silva, B., Marques, S.A., et al., 2024. NMDA receptor remodeling and nNOS activation in mice after unilateral striatal injury with 6-OHDA. Heliyon 10 (14), e34120.
Deng, D., Masri, S., Yao, L., et al., 2020. Increasing endogenous activity of NMDARs on GABAergic neurons increases inhibition, alters sensory processing and prevents noise-induced tinnitus. Sci. Rep. 10 (1), 11969.
Du, Y., Huang, Z., Wu, Y., et al., 2024. Glymphatic system dysfunction associated with cognitive impairment in chronic tinnitus patients. Front Neurosci. 18, 1455294.
Engelke, M., Simões, J.P., Basso, L., et al., 2025. Understanding tinnitus symptom dynamics and clinical improvement through intensive longitudinal data. NPJ Digit Med 8 (1), 27.
Engineer, N.D., Riley, J.R., Seale, J.D., et al., 2011. Reversing pathological neural activity using targeted plasticity. Nature 470 (7332), 101–104.
Feng, Y., Huang, Z., Ma, X., et al., 2024. Activation of testosterone-androgen receptor mediates cerebrovascular protection by photobiomodulation treatment in photothrombosis-induced stroke rats. CNS Neurosci. Ther. 30 (2), e14574.
Galazyuk, A., Hébert, S., 2015. Gap-prepulse inhibition of the Acoustic Startle Reflex (GPIAS) for tinnitus assessment: current status and future directions. Front Neurol. 6, 88.
Hamblin, M.R., 2024. Transcranial photobiomodulation for the brain: a wide range of clinical applications. Neural Regen. Res 19 (3), 483–484.

Han, Y., Wei, Z.Y., Zhao, N., et al., 2025. Transcranial magnetic stimulation in attention-deficit/hyperactivity disorder: a systematic review and meta-analysis of cortical excitability and therapeutic efficacy. Front Psychiatry 16, 1544816.
Hayes, S.H., Patel, S.V., Arora, P., et al., 2024. Neurophysiological, structural, and molecular alterations in the prefrontal and auditory cortices following noise-induced hearing loss. Neurobiol. Dis. 200, 106619.
Hong, N., Kim, H.J., Kang, K., et al., 2023. Photobiomodulation improves the synapses and cognitive function and ameliorates epileptic seizure by inhibiting downregulation of Nlgn3. Cell Biosci. 13 (1), 8.
Hong, N., Yoon, S.R., Ahn, J.C., 2025. Photobiomodulation using an 830-nm laser alleviates hippocampal reactive gliosis and cognitive dysfunction in a mouse model of adolescent chronic alcohol exposure. Pharm. Biochem Behav. 248, 173956.
Huang, Y.Y., Nagata, K., Tedford, C.E., et al., 2014. Low-level laser therapy (810 nm) protects primary cortical neurons against excitotoxicity in vitro. J. Biophotonics 7 (8), 656–664.
Karreman, M.A., Venkataramani, V., 2025. Calm in the chaos: Targeting mTOR to reduce glioma-driven neuronal hyperexcitability. Neuron 113 (6), 795–797.
Kim, Y.R., Jun, S., Jung, S., et al., 2025. Inhibition of the mitochondrial permeability transition pore as a promising target for protecting auditory function in cisplatin-induced hearing loss. Biomed. Pharm. 182, 117767.
Korkmaz, H., Anstötz, M., Wellinghof, T., et al., 2025. Loss of Bmal1 impairs the glutamatergic light input to the SCN in mice. Front Cell Neurosci. 19, 1538985.
Kraus, K.S., Mitra, S., Jimenez, Z., et al., 2010. Noise trauma impairs neurogenesis in the rat hippocampus. Neuroscience 167 (4), 1216–1226.
Kweon, J., Vigne, M.M., Jones, R.N., et al., 2023. Practice makes plasticity: 10-Hz rTMS enhances LTP-like plasticity in musicians and athletes. Front Neural Circuits 17, 1124221.
Langguth, B., De Ridder, D., Schlee, W., et al., 2024. Tinnitus: Clinical Insights in Its Pathophysiology-A Perspective. J. Assoc. Res Otolaryngol. 25 (3), 249–258.
Latchoumane, C.V., Jackson, L., Sendi, M.S.E., et al., 2018. Chronic Electrical Stimulation Promotes the Excitability and Plasticity of ESC-derived Neurons following Glutamate-induced Inhibition In vitro. Sci. Rep. 8 (1), 10957.
Li, S., Choi, V., Tzounopoulos, T., 2013. Pathogenic plasticity of Kv7.2/3 channel activity is essential for the induction of tinnitus. Proc. Natl. Acad. Sci. USA 110 (24), 9980–9985.
Liu, P., Xue, X., Zhang, C., et al., 2024. Mid-Infrared Photons Alleviate Tinnitus by Activating the KCNQ2 Channel in the Auditory Cortex. Res. (Wash. D. C.) 7, 0479.
Longenecker, R.J., Kristaponyte, I., Nelson, G.L., et al., 2018. Addressing variability in the acoustic startle reflex for accurate gap detection assessment. Hear Res 363, 119–135.
Meng, P., Zhang, X., Liu, T.T., et al., 2023. A whole transcriptome profiling analysis for antidepressant mechanism of Xiaoyaosan mediated synapse loss via BDNF/trkB/PI3K signal axis in CUMS rats. BMC Complement Med Ther. 23 (1), 198.
Miwa, T., Kanai, R., Kanemaru, S.I., 2023. Long-term exposure to high-concentration dexamethasone in the inner ear via intratympanic administration. Steroids 189, 109152.
Mohammed, H.S., Khadrawy, Y.A., 2022. Antidepressant and antioxidant effects of transcranial irradiation with 830-nm low-power laser in an animal model of depression. Lasers Med Sci. 37 (3), 1615–1623.
Nam, C.I., Chen, L., 2005. Postsynaptic assembly induced by neurexin-neuroligin interaction and neurotransmitter. Proc. Natl. Acad. Sci. USA 102 (17), 6137–6142.
Rafe, M.R., Saha, P., Bello, S.T., 2024. Targeting NMDA receptors with an antagonist is a promising therapeutic strategy for treating neurological disorders. Behav. Brain Res 472, 115173.
Rosická, A.M., Teckentrup, V., Fittipaldi, S., et al., 2024. Modifiable dementia risk factors associated with objective and subjective cognition. Alzheimers Dement 20 (11), 7437–7452.
Schilling, A., Krauss, P., Gerum, R., et al., 2017. A New Statistical Approach for the Evaluation of Gap-prepulse Inhibition of the Acoustic Startle Reflex (GPIAS) for Tinnitus Assessment. Front Behav. Neurosci. 11, 198.
Sherlock, L.P., Ballard-Hernandez, J., Boudin-George, A., et al., 2025. Clinical Practice Guideline for Management of Tinnitus: Recommendations From the US VA/DOD Clinical Practice Guideline Work Group. JAMA Otolaryngol. Head. Neck Surg.
Song, A., Cho, G.W., Vijayakumar, K.A., et al., 2021. Neuroprotective effect of valproic acid on salicylate-induced tinnitus. Int J. Mol. Sci. 23 (1).
Stebbing, A.R., 1982. Hormesis–the stimulation of growth by low levels of inhibitors. Sci. Total Environ. 22 (3), 213–234.
Stevens, A.R., Hadis, M., Thareja, A., et al., 2025. Photobiomodulation improves functional recovery after mild traumatic brain injury. Bioeng. Transl. Med 10 (2), e10727.
Sun, M.J., Ren, W.J., Zhao, Y.F., et al., 2025. Hippocampal P2X7 and A2A purinoceptors mediate cognitive impairment caused by long-lasting epileptic seizures. Theranostics 15 (7), 3159–3184.
Turner, J.G., Brozoski, T.J., Bauer, C.A., et al., 2006. Gap detection deficits in rats with tinnitus: a potential novel screening tool. Behav. Neurosci. 120 (1), 188–195.
Wang, L., Mao, L., Huang, Z., et al., 2025. Photobiomodulation: shining a light on depression. Theranostics 15 (2), 362–383.
Wood, R.L., Calvo, P.M., Mccallum, W.M., et al., 2025. GABA and Glycine Synaptic Release on Axotomized Motoneuron Cell Bodies Promotes Motor Axon Regeneration. Eur. J. Neurosci. 61 (5), e70045.
Xie, J., Zhang, W., Wei, W., et al., 2025. The Alteration of Brain Network Topology in Tinnitus Transition From Recent-Onset to Chronic. Eur. J. Neurosci. 61 (2), e16664.
Xiong, X.R., Liang, F., Zingg, B., et al., 2015. Auditory cortex controls sound-driven innate defense behaviour through corticofugal projections to inferior colliculus. Nat. Commun. 6, 7224.
Yang, Y., Yuan, S., Lin, H., et al., 2025. Potential locations for non-invasive brain stimulation in treating ADHD: Results from a cross-dataset validation of functional connectivity analysis. Transl. Psychiatry 15 (1), 81.
Yang, Z.H., Cai, X., Zhang, C.Y., et al., 2024. NEK4 modulates circadian fluctuations of emotional behaviors and synaptogenesis in male mice. Nat. Commun. 15 (1), 9180.
Yao, P.T., Shen, J., Chen, L., et al., 2019. Cortical ensemble activity discriminates auditory attentional states. Mol. Brain 12 (1), 80.
Yi, B., Wu, C., Shi, R., et al., 2018. Long-term Administration of Salicylate-induced Changes in BDNF Expression and CREB Phosphorylation in the Auditory Cortex of Rats. Otol. Neurotol. 39 (3), e173–e180.
Yu, T., Cui, J., Chen, S., 2024. Electrochemical detection of the neurotransmitter glutamate and the effect of the psychotropic drug riluzole on its oxidation response. Anal. Bioanal. Chem. 416 (7), 1707–1716.
Zhang, H., Ben Zablah, Y., Zhang, H., et al., 2022b. Inhibition of Rac1 in ventral hippocampal excitatory neurons improves social recognition memory and synaptic plasticity. Front Aging Neurosci. 14, 914491.
Zhang, L., Wu, C., Martel, D.T., et al., 2021. Noise Exposure Alters Glutamatergic and GABAergic Synaptic Connectivity in the Hippocampus and Its Relevance to Tinnitus. Neural Plast. 2021, 8833087.
Zhang, M., Feng, J., Xie, C., et al., 2025. Assembly and architecture of endogenous NMDA receptors in adult cerebral cortex and hippocampus. Cell 188 (5), 1198–1207 e13.
Zhang, X., Wu, W., Luo, Y., et al., 2022a. Transcranial Photobiomodulation therapy ameliorates perioperative neurocognitive disorder through modulation of mitochondrial function in aged mice. Neuroscience 490, 236–249.